The Astrophysical Journal, 968:74 (25pp), 2024 June 20 https://doi.org/10.3847/1538-4357/ad3fb5
© 2024. The Author(s). Published by the American Astronomical Society.
OPEN ACCESS

ICM-SHOX. I. Methodology Overview and Discovery of a Gas–Dark Matter Velocity Decoupling in the MACS J0018.5+1626 Merger

Emily M. Silich[1,2], Elena Bellomi[2], Jack Sayers[1], John ZuHone[2], Urmila Chadayammuri[3], Sunil Golwala[1], David Hughes[4], Alfredo Montaña[4], Tony Mroczkowski[5], Daisuke Nagai[6], David Sánchez-Argüelles[7], S. A. Stanford[8], Grant Wilson[9], Michael Zemcov[10], and Adi Zitrin[11]

[1] Cahill Center for Astronomy and Astrophysics, California Institute of Technology, Pasadena, CA 91125, USA
[2] Center for Astrophysics | Harvard & Smithsonian, 60 Garden St., Cambridge, MA 02138, USA
[3] Max Planck Institut für Astronomie, Königstuhl 17, 69121 Heidelberg, Germany
[4] Instituto Nacional de Astrofísica, Óptica, y Electrónica (INAOE), Aptdo. Postal 51 y 216, 7200, Puebla, Mexico
[5] European Southern Observatory, Karl-Schwarzschild-Str. 2, D-85748, Garching, Germany
[6] Physics Department, Yale University, New Haven, CT 06520, USA
[7] Consejo Nacional de Ciencia y Tecnología-Instituto Nacional de Astrofísica, Óptica, y Electrónica (CONACyT-INAOE), Luis Enrique Erro 1, 72840 Puebla, Mexico
[8] Department of Physics and Astronomy, University of California, Davis, CA 95616, USA
[9] University of Massachusetts, Amherst, MA 01003, USA
[10] Rochester Institute of Technology, Rochester, NY 14623, USA
[11] Ben-Gurion University of the Negev, P.O. Box 653, Be'er-Sheva 8410501, Israel; esilich@caltech.edu
Received 2023 September 21; revised 2024 April 4; accepted 2024 April 4; published 2024 June 12

Abstract

Galaxy cluster mergers are rich sources of information to test cluster astrophysics and cosmology. However, cluster mergers produce complex projected signals that are difficult to interpret physically from individual observational probes. Multi-probe constraints on the gas and dark matter (DM) cluster components are necessary to infer merger parameters that are otherwise degenerate. We present Improved Constraints on Mergers with SZ, Hydrodynamical simulations, Optical, and X-ray (ICM-SHOX), a systematic framework to jointly infer multiple merger parameters quantitatively via a pipeline that directly compares a novel combination of multi-probe observables to mock observables derived from hydrodynamical simulations. We report a first application of the ICM-SHOX pipeline to MACS J0018.5+1626, wherein we systematically examine simulated snapshots characterized by a wide range of initial parameters to constrain the MACS J0018.5+1626 merger geometry. We constrain the epoch of MACS J0018.5+1626 to the range 0–60 Myr post-pericenter passage, and the viewing angle is inclined ≈27°–40° from the merger axis. We obtain constraints for the impact parameter ($\lesssim$250 kpc), mass ratio (≈1.5–3.0), and initial relative velocity when the clusters are separated by 3 Mpc (≈1700–3000 km s^{-1}). The primary and secondary clusters initially (at 3 Mpc) have gas distributions that are moderately and strongly disturbed, respectively. We discover a velocity space decoupling of the DM and gas distributions in MACS J0018.5+1626, traced by cluster-member galaxy velocities and the kinematic Sunyaev–Zel'dovich effect, respectively. Our simulations indicate this decoupling is dependent on the different collisional properties of the two distributions for particular merger epochs, geometries, and viewing angles.

Unified Astronomy Thesaurus concepts: Galaxy clusters (584); Intracluster medium (858); Hydrodynamical simulations (767); Observational cosmology (1146); X-ray astronomy (1810); Sunyaev-Zeldovich effect (1654); Galaxy spectroscopy (2171); Strong gravitational lensing (1643)

Supporting material: animations, machine-readable tables

1. Introduction

The standard Λ cold dark matter (ΛCDM) cosmological model predicts that structures in the universe form hierarchically (e.g., Springel et al. 2005). In the early universe, weak positive fluctuations in the cosmic density field formed small overdensities, which overcame cosmic expansion and collapsed via gravity. From these density perturbations, larger structures form throughout cosmic time by merging and smooth accretion. The current ($z \sim 0$) stage of cosmological structure formation in the universe is the formation and growth of galaxy clusters.[12] With total masses of $\sim 10^{14}$–$10^{15} M_\odot$, galaxy clusters comprise two main mass components: dark matter (DM; ∼80%–90% of the total mass) and baryonic matter (∼10%–20%), which is dominated by hot, diffuse plasma in the intracluster medium (ICM; see Voit 2005; Kravtsov & Borgani 2012, for reviews).

While some growth of galaxy clusters can be attributed to the smooth accretion of streams of material from the cosmic web and lower mass structures (e.g., galaxies), the primary hierarchical growth mechanism of clusters is major mergers between similar mass systems (Muldrew et al. 2015; Molnar 2016). Such events can drive bulk motions and large-scale turbulence in the ICM with velocities of $\sim 10^3$ km s^{-1} and heat the gas up to temperatures of $\sim 10^7$–10^8 K (Markevitch & Vikhlinin 2007). Studies of galaxy clusters can, therefore, play two key scientific roles. First, because of the enormous scales of distance (a few megaparsecs; Voit 2005) and energy ($\lesssim 10^{64}$ erg; Molnar 2016) that clusters probe, generic physical processes like turbulence, shocks, and accretion play out to an unprecedented degree in mergers. Consequently, complementary observational

[12] As the expansion of the Universe continues to accelerate under the standard ΛCDM model, the largest expected virialized structures are only a few times larger than the most massive clusters currently known (e.g., Araya-Melo et al. 2009).

Original content from this work may be used under the terms of the Creative Commons Attribution 4.0 licence. Any further distribution of this work must maintain attribution to the author(s) and the title of the work, journal citation and DOI.

Table 1
Details of the Galaxy Clusters in ICM-SHOX[a]

Cluster Name	R.A.	Decl.	z	M_{500} ($10^{14}\ M_{\odot}$)	Dynamical State
A0697	$08^h42^m57.^s6$	$+36°21'57''$	0.28	17.1	Likely LOS merger
A1835	$14^h01^m01.^s9$	$+02°52'40''$	0.25	12.3	Relaxed
MACS J0018.5+1626	$00^h18^m33.^s4$	$+16°26'13''$	0.55	16.5	Likely LOS merger
MACS J0025.4-1222	$00^h25^m29.^s9$	$-12°22'45''$	0.58	7.6	Likely POS merger
MACS J0454.1-0300	$04^h54^m11.^s4$	$-03°00'51''$	0.54	11.5	Likely POS merger
MACS J0717.5+3745	$07^h17^m32.^s1$	$+37°45'21''$	0.55	24.9	Likely LOS merger
MACS J2129.4-0741	$21^h29^m25.^s7$	$-07°41'31''$	0.59	10.6	Likely LOS merger
RX J1347.5-1145	$13^h47^m30.^s8$	$-11°45'09''$	0.45	21.7	Likely POS merger

Note.
[a] Summarized from Table 1 of Sayers et al. (2019) and references therein.

and simulation-based studies of major mergers are a powerful means to further our understanding of these ubiquitous physical phenomena and the role they play in cosmological structure formation. Second, population statistics of major mergers between massive clusters of galaxies are a sensitive diagnostic of the underlying cosmological model (e.g., Lacey & Cole 1993; Fakhouri et al. 2010; Thompson & Nagamine 2012). For example, major mergers trace the velocity distribution of halos at the extreme end of the mass function, so observed velocities from well-characterized samples can be compared to velocity distribution predictions derived from cosmological simulations in order to test various cosmological parameterizations (Molnar 2016). Exceptional mergers (e.g., the "Bullet Cluster" 1E 0657-558; Markevitch et al. 2002) have the potential to provide powerful tests of the ΛCDM paradigm, and much simulation work has been undertaken to understand the cosmological implications of these mergers (see Thompson et al. 2015).

Observational diagnostics of galaxy cluster mergers have included X-ray imaging and spectroscopy, gravitational lensing (GL) mass reconstructions, radio relics, thermal Sunyaev–Zel'dovich (tSZ) effect imaging, and positional offsets between these observables (Clowe et al. 2006; van Weeren et al. 2010; Molnar et al. 2012; Molnar 2016; Di Mascolo et al. 2021; Russell et al. 2022), which can generally be reproduced by both cosmological and idealized simulations (see ZuHone et al. 2018). However, observational comparisons to simulations have primarily been limited in two ways. Most analyses involve only a single object because of the need for deep, multi-probe data in order to characterize a merger adequately. Furthermore, these analyses focus on mergers occurring in or near the plane-of-sky (POS), so that the morphological signatures associated with the merger can be clearly identified, thus making them more straightforward to interpret. To overcome these limitations, one can also make use of line-of-sight (LOS) velocity information, which expands the set of mergers that can be analyzed and may also be critical to obtaining conclusive results from comparisons to simulations (e.g., Chadayammuri et al. 2022).

LOS velocity information in mergers has typically been obtained from redshifts of cluster-member galaxies, which are believed to reliably trace the DM distribution (Ma et al. 2009; Owers et al. 2011; Boschin et al. 2013). However, as mergers evolve, the DM velocities are expected to decouple from the ICM velocities, since the collisional ICM is affected by hydrodynamical processes, while the DM is collisionless, interacting only via gravity (Poole et al. 2006). While the existence of a velocity space difference between the ICM and DM can be inferred from positional offsets of the two components (e.g., Merten et al. 2011), a direct measurement of this velocity decoupling has not yet been achieved observationally, since this requires spatially resolved measurements of both the ICM and DM LOS velocities. In the X-ray band, such observations can be carried out with microcalorimeter instruments, as shown by the observations of bulk velocities in the Perseus cluster with Hitomi (Hitomi Collaboration et al. 2016, 2018). While this technique will be made available by upcoming instruments on XRISM (XRISM Science Team 2020), Athena (Barret et al. 2020), and LEM (Kraft et al. 2022), it is not currently available. Recently, ICM LOS velocities of individual clusters have been measured using the kinematic Sunyaev–Zel'dovich (kSZ) effect (Sayers et al. 2013; Adam et al. 2017; Sayers et al. 2019), which is a Doppler shift of the cosmic microwave background (CMB) signal due to the bulk motion of galaxy clusters (Sunyaev & Zeldovich 1980; see Mroczkowski et al. 2019 for a review). By incorporating LOS ICM velocities derived from current kSZ measurements, it is now possible to directly probe both the POS morphology and LOS velocity features of both mass components (DM and ICM) in mergers.

In this paper, we introduce the Improved Constraints on Mergers with SZ, Hydrodynamical simulations, Optical, and X-ray (ICM-SHOX) sample, which comprises a set of deep, multi-probe data for eight massive, intermediate-redshift galaxy clusters. From these data, we are able to characterize the POS morphology and LOS velocity structure of the constituent ICM and DM components for the first time in such a merger analysis. ICM-SHOX contains four galaxy cluster mergers likely occurring primarily along the LOS, three mergers likely occurring in the POS, and one relaxed object as a control (see Table 1). The quality of these multi-probe data is relatively uniform across each object in the sample. The ICM-SHOX sample consists primarily of exceptional (e.g., high-mass, actively merging) objects, which allows us to test for deviations from ΛCDM in the most extreme regime of structure growth in the universe.

In order to determine the geometry of these mergers and obtain robust population statistics of cluster component masses, gas profiles, initial impact parameters, initial relative velocities, merger epochs, and viewing angles, we compare observables derived from the multi-probe data to analogous mock observables generated with tailored idealized hydrodynamical binary galaxy cluster merger simulations. We have developed an automated pipeline that enables us to reduce the observational data for each cluster, generate analogous mock

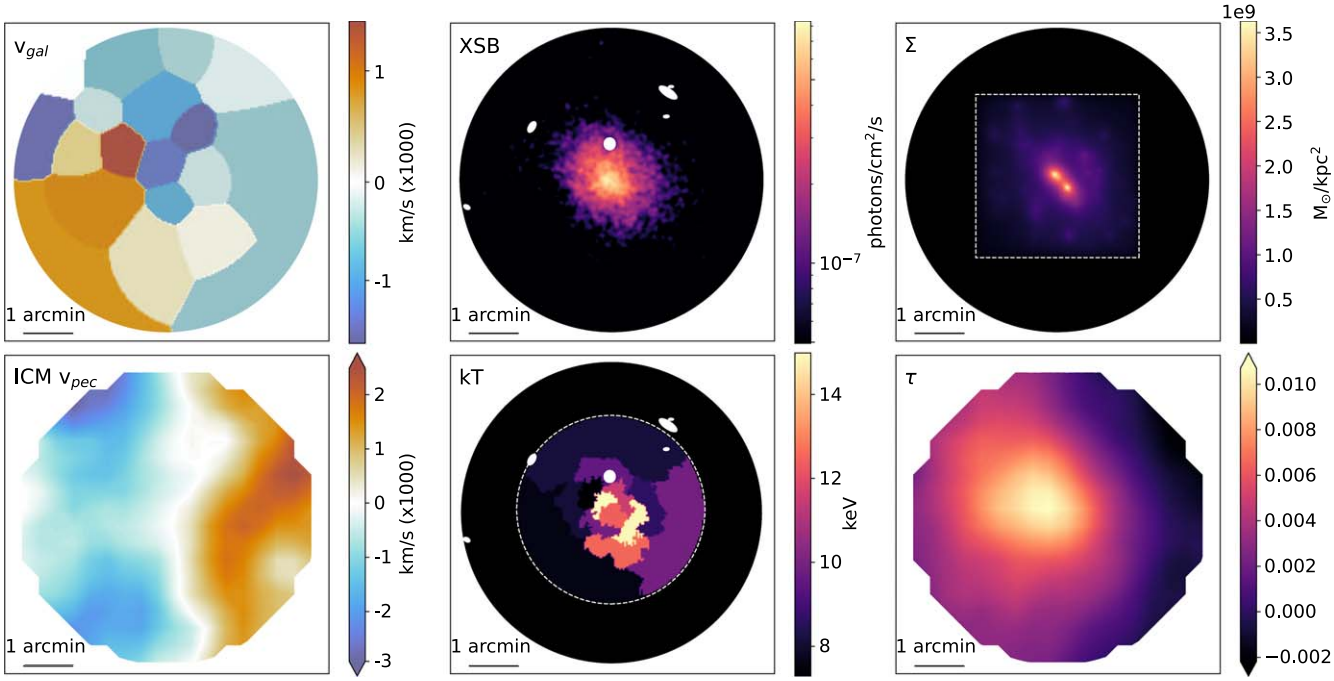

Figure 1. MACS J0018.5+1626 multi-probe observations: top row, from left: LOS galaxy velocities ($v_{\rm gal}$), XSB, GL projected total mass (Σ); bottom row, from left: LOS ICM velocities (ICM $v_{\rm pec}$), X-ray derived temperatures (kT), LOS ICM electron optical depth (τ).

observables from simulations characterized by a vast array of initial parameters, and directly compare the data sets. Our framework then jointly infers the above merger parameters for each cluster quantitatively via a frequentist statistical analysis. In this study, we demonstrate the capabilities of this pipeline applied to our novel combination of multi-probe data for one member of ICM-SHOX, MACS J0018.5+1626.

In Section 2, we describe the observational data for the full ICM-SHOX sample and detail the data reduction and analysis procedures for MACS J0018.5+1626. Section 3 contains an overview of the hydrodynamical simulations we employ and describes our process of generating mock observables for direct comparison to the observational data. In Sections 4 and 5, we describe methods for constraining the MACS J0018.5+1626 merger parameters with the ICM-SHOX pipeline and the resulting constraints, respectively. Section 6 contains a detailed simulation-based exploration of the decoupling between the gas and DM velocity structure observed in MACS J0018.5+1626. We give conclusions and applications to the full ICM-SHOX sample in Section 7. We assume a spatially flat ΛCDM cosmology with $H_0 = 70$ km s^{-1} Mpc^{-1} and $\Omega_{m,0} = 0.3$, unless otherwise specified.

2. Observational Data

2.1. The ICM-SHOX Sample

For each object in the sample, we characterize the POS DM morphology using projected total mass (Σ) maps from strong GL models fit to imaging data from the Hubble Space Telescope (HST; e.g., Zitrin et al. 2011, 2015). The POS ICM morphology is described by two observables. First, we construct X-ray surface brightness (XSB) and temperature (kT) maps using observations taken with the Chandra X-ray Observatory. Then, we obtain projected ICM density maps using the SZ effect (Sayers et al. 2019) measured via a combined analysis of data from Bolocam, AzTEC, and Planck. The LOS DM velocity is traced using spectroscopic redshifts ($z_{\rm spec}$) of cluster-member galaxies obtained primarily with the DEIMOS instrument (Faber et al. 2003) at the Keck Observatory. We characterize the LOS ICM velocity (ICM $v_{\rm pec}$) using projected ICM velocity maps from the SZ effect, again based on an analysis of Bolocam, AzTEC, and Planck observations (Sayers et al. 2019).

Each data set probes $>3'$ from the center of the cluster, with the exception of the GL maps (which are limited by the HST field of view) and the kT maps (which are only constructed within a central region where the cluster counts are comparable to background counts; see Section 2.2). At the redshift of the ICM-SHOX sample, this angular extent corresponds to $\sim$1 Mpc in the POS, which is typically large enough to capture primary features of the merger (e.g., separate cluster mass peaks and merger-driven shocks). In this analysis, we focus on one member of the ICM-SHOX sample, MACS J0018.5+1626, which is a massive, extensively studied cluster merger (see, e.g., Solovyeva et al. 2007) at $z = 0.546$ (Ebeling et al. 2007) that is likely elongated along the LOS (Piffaretti et al. 2003; Sayers et al. 2019). We describe each observational data set (see Figure 1) and corresponding data processing for MACS J0018.5+1626 below.

2.2. X-Ray

The X-ray data reduction was performed with `CIAO` version 4.14 (Fruscione et al. 2006). MACS J0018.5+1626 observations correspond to Chandra ObsId 520, doi:10.25574/00520. The raw ACIS-I data for ObsID 520 were calibrated using the CalDB version 4.9.4 with `chandra_repro`. The data were exposure-corrected with `fluximage`. Point sources were identified using the `CIAO` implementation of a wavelet source detection method (`wavdetect`; Freeman et al. 2002) and excluded from the exposure-corrected images. The light curve was flare-filtered with `deflare` to identify good time intervals

(GTI), which were applied to the data. The total GTI after data filtering is 63.8 ks. We used the `flux_obs` tool to generate a filtered, exposure-corrected 0.5–7 keV XSB map free of point sources, which, having 1.7×10^4 source counts, is sufficiently deep to resolve morphological features.

The `blanksky` routine was used to construct blank-sky background event files scaled and reprojected to match the MACS J0018.5+1626 data. Since they are derived from deep, point source-free observations averaged across large regions of the sky, the background files nominally account for contributions from the particle-induced instrumental background (Bartalucci et al. 2014), as well as astrophysical foreground components (e.g., the Local Hot Bubble and the hot Galactic halo) and background components (e.g., the contributions from unresolved extragalactic point sources to the cosmic X-ray background).

In order to generate robust kT maps, we first identified a circular region centered on MACS J0018.5+1626, within which the cluster source counts ($N_{\rm cluster}$) are comparable to or larger than the background counts within each pixel ($N_{\rm BKG}$). We estimated $N_{\rm cluster} + N_{\rm BKG}$ for each pixel in the 0.5–7 keV filtered events image (binned to a pixel size of 4″ to reduce statistical variation between pixels), and we derived $N_{\rm BKG}$ with the analogously binned blank-sky background image. The resulting circular region within which $N_{\rm source} \sim N_{\rm BKG}$ for $\gtrsim$75% of the pixels has $r = 1\farcm8$.

Then, the 0.5–7 keV filtered events image was contour binned within the $1\farcm8$; circular region using the `contbin` algorithm (Sanders 2006). The 0.5–7 keV blank-sky background image was specified for the signal-to-noise ratio (S/N) calculations used to determine the bin edges. We extracted source spectra from the filtered event file and background spectra from the blank-sky event file for each of the regions defined by the contour bins with `specextract`. We tailored the contour binning algorithm input parameters so each cluster bin has ∼1000 counts after the blank-sky background subtraction to maximize the kT map spatial resolution while maintaining sufficient counts to obtain a high-quality spectral fit. Each extracted spectrum was binned to have a minimum of 25 counts per spectral bin to allow the use of χ^2 statistics in the spectral fitting.

All spectral fitting was performed with `sherpa` over an energy range of 0.5–7 keV. The blank-sky background-subtracted cluster bins were fit with a model for a single collisionally ionized plasma modified by interstellar absorption (`tbabs` × `apec`; Wilms et al. 2000; Smith et al. 2001) with fixed $n_{\rm H} = 4 \times 10^{20}$ cm^{-2} (HI4PI Collaboration et al. 2016), $z = 0.546$, and $Z = 0.3\,Z_\odot$ using abundances from Anders & Grevesse (1989). The plasma temperature and normalization were fit as free parameters. For MACS J0018.5+1626, the contour binning produces 14 spatial bins within $1\farcm8$ of the cluster center, within which temperature enhancements due to shocks produced in the merger are easily identifiable.

We then inspected the MACS J0018.5+1626 XSB and kT maps for discontinuities associated with merger-driven shocks, which, if present, could be used to help constrain the merger geometry (e.g., Markevitch et al. 2002) and evolutionary state (e.g., Russell et al. 2012). We first applied a Gaussian gradient magnitude filter (Sanders et al. 2016a, 2016b) to the MACS J0018.5+1626 XSB map and identified enhancements that would be indicative of merger-driven shocks. For each of these enhancements, we generated radial surface brightness profiles and inspected them for evidence of surface brightness jumps. In a study of the A2256 merger, Breuer et al. (2020) note that for highly inclined mergers (occurring near the LOS), temperature jumps can be more reliable indicators of the presence of a shock front. Therefore, in any regions that indicated the possible presence of a radial surface brightness jump, we fit downstream and upstream plasma temperatures to photons extracted from regions below and above the jump position, respectively. We applied the Rankine–Hugoniot jump conditions as a function of Mach number for the ratio of the downstream and upstream plasma temperatures across a plane-parallel shock (Landau & Lifshitz 1959) to each enhancement-identified region of interest. Within uncertainties, all Mach numbers were consistent with one (i.e., no shock). Given our relatively low S/N, we do not use the presence (or lack) of clear shocks in the X-ray observables as a diagnostic of the merger geometry.

2.3. GL

The projected total mass distribution of MACS J0018.5+1626 was modeled using the Light Traces Mass (LTM) GL approach of Zitrin et al. (2015) applied to HST imaging. A full description of the method is given in Zitrin et al. (2015); in short, the LTM model assumes that cluster-member galaxy masses scale like their luminosities, and the total DM distribution follows a similar shape, so that it can be represented by a smoothed map of the cluster-member galaxies. The model is constrained by minimizing the distances of predicted multiple images from their actual observed locations with a Markov Chain Monte Carlo (MCMC) minimization utilizing a χ^2 function.

A preliminary strong lensing model of MACS J0018.5+1626 based on older HST data was detailed in Zitrin et al. (2011). Here, we use a revised model that incorporates publicly available Very Large Telescope/MUSE data (Program ID 0103.A-0777(B), PI: Edge) as well as dedicated Gemini/GNIRS data (Program ID: GN-2021B-Q-903, PI: Zitrin) for the cluster. These data reveal UV and optical emission lines as well as a (double-peaked) Lyα line at $z = 3.21$ for the main lensed system (Furtak et al. 2022). HST imaging data from the RELICS survey (Coe 2016; Coe et al. 2019) has yielded two new multiple-image systems, which are also incorporated in the revised version. In total, the current model, which is similar to the one presented in Furtak et al. (2022), has 10 free parameters and uses six sets of multiple image constraints from five background galaxies up to redshift $z \sim 5$ as constraints. The final image reproduction rms of the model is 0″.86. In the resulting projected total mass distribution map, two primary mass peaks are clearly identifiable.

2.4. SZ Effect

Sayers et al. (2019) produced projected LOS ICM density and velocity maps for each merger in our sample, including MACS J0018.5+1626, using SZ effect observations from Bolocam, AzTEC, and Planck. The data were used to generate SZ effect maps at 140 and 270 GHz with a common point-spread function with a full width at half-maximum ($\rm PSF_{FWHM}$) of 70″. The data from Planck were used solely to set the absolute additive normalization of the SZ effect maps, since, while the ground-based data provide much better angular resolution than Planck, the data processing procedures required

to subtract atmospheric fluctuations also remove the normalization information. The 140 and 270 GHz data were combined with an X-ray-derived kT map to produce the LOS ICM density and velocity maps. We note that the kT map used in the SZ analysis is derived from the same data as the MACS J0018.5+1626 kT map generated in this work (see Section 2.2) but was calculated with an older X-ray analysis procedure. Differences between the X-ray reduction used by Sayers et al. (2019) and that employed in the current work produce negligible changes in the SZ-derived quantities relative to the measurement noise. The S/N for the ICM density map is ∼5–10, and the uncertainty within each 70″ resolution element in the ICM $v_{\rm pec}$ map is $\sim 1000\ {\rm km\,s^{-1}}$.

2.5. Cluster-member Optical Spectroscopy

Previous studies have shown that averaging redshifts of cluster-member galaxies is a useful measure of the bulk LOS DM velocity structure in a galaxy cluster (e.g., Boschin et al. 2006; Ma et al. 2009; Dehghan et al. 2017). Furthermore, cosmological simulations have indicated that the bias between the velocity dispersions of cluster-member galaxies and DM is relatively low (Anbajagane et al. 2022). Therefore, throughout this work, we assume that the LOS cluster-member galaxy velocities trace the LOS DM velocity structure.

We have combined both existing literature catalogs (Dressler & Gunn 1992; Ellingson et al. 1998; Crawford et al. 2011) with new DEIMOS observations obtained by our group to collect 156 cluster-member $z_{\rm spec}$ across the face of MACS J0018.5+1626 within a $6\farcm7 \times 6\farcm7$ region around the cluster center. The DEIMOS data which were observed prior to 2021 August were reduced with the `spec2d` DEIMOS data reduction pipeline (Cooper et al. 2012; Newman et al. 2013), and those observed from 2021 August onward were reduced with a modern Python implementation of the DEIMOS data reduction pipeline (`PypeIt`; Prochaska et al. 2020). We used `SpecPro` (Masters & Capak 2011) to extract redshifts from the 1D reduced cluster-member galaxy spectra by identifying either the Ca II H+K absorption lines or the [O II] 3727 Å doublet, with some objects additionally showing the Hδ- and G-band absorption lines. We provide tables of the MACS J0018.5+1626 literature cluster-member redshifts, as well as (non-) cluster-member redshifts that were observed in our Keck program in Appendix C (Tables C1–C3).

Next, we converted each redshift relative to the median redshift of the cluster (0.546) to a velocity relative to the average SZ-derived bulk ICM LOS velocity of MACS J0018.5+1626 ($v_{\rm bulk} \simeq -100\ {\rm km\,s^{-1}}$; Sayers et al. 2019). In other words, we define a cluster-member galaxy at $z = 0.546$ to be at rest relative to the bulk ICM LOS velocity. We thus enforce that the overall average observed bulk velocity of the ICM and the DM are equal. Then, we applied the weighted Voronoi tessellation (WVT) algorithm of Diehl & Statler (2006) to bin the cluster-member velocities within the $6\farcm7 \times 6\farcm7$ region into a high-fidelity spatial map. We use a publicly available Python implementation of the WVT algorithm (XtraAstronomy/Pumpkin; Rhea et al. 2020) for the spatial binning, and we apply estimators from Beers et al. (1990) to calculate the velocity ($v_{\rm gal}$) within each spatial bin. The MACS J0018.5+1626 LOS galaxy velocity map has 19 spatial bins across the face of the cluster.

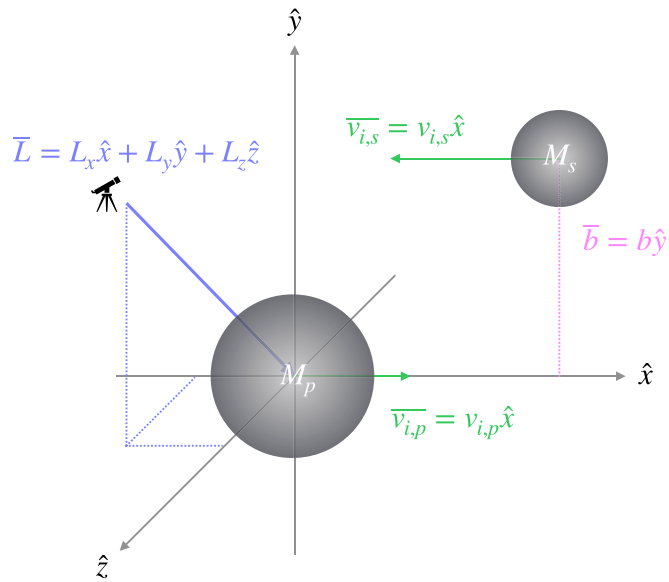

Figure 2. Schematic of the merger geometry initial configuration (based on Figure 1 of Chadayammuri et al. 2022). $M_{\rm P}$ and $M_{\rm S}$ are the primary and secondary cluster masses, respectively. b is the impact parameter (defined along the $\hat{y}$ axis). $v_{i,p}$ and $v_{i,s}$ are the primary and secondary cluster initial velocities (defined in the $\hat{x}$ axis), where $v_i = |v_{i,p} - v_{i,s}|$. $\boldsymbol{L}$ is the viewing angle vector for simulation projections, defined with components in ($\hat{x}$, $\hat{y}$, $\hat{z}$).

3. Hydrodynamical Binary Merger Simulations

3.1. Simulated Data Sets

We generate simulated observables analogous to the multi-probe MACS J0018.5+1626 data by tailoring a suite of idealized hydrodynamical galaxy cluster merger simulations, after the manner of previous works (e.g., Ricker & Sarazin 2001; Poole et al. 2006; ZuHone 2011; Chadayammuri et al. 2022). We use the GPU-accelerated code GAMER-2 (Schive et al. 2018) to run the simulations, which solves the equations of hydrodynamics, N-body interactions, and gravity on an adaptive mesh refinement (AMR) grid. Each simulation is initialized as a binary cluster merger for a given choice of total mass, mass ratio $R = M_{\rm P}/M_{\rm S}$ of the primary to the secondary cluster (where both masses are defined as the enclosed mass within the cluster's r_{200c}), impact parameter b, and relative velocity of the infalling galaxy clusters v_i.

We define the total MACS J0018.5+1626 mass derived from the GL mass reconstruction map ($M_{500} = 1.1 \times 10^{15}\ M_\odot$) in all simulations and use this to scale the masses of the two clusters pre-merger. We note that this GL mass estimate is lower than that derived from an X-ray scaling relation (see Table 1). However, we select the GL mass estimate for our simulations since using the X-ray derived mass estimate results in inconsistencies when comparing the total surface density maps.

The clusters are initially separated by a distance of 3 Mpc, and v_i is defined along the merger axis ($\hat{x}$) while b is defined along the orthogonal $\hat{y}$ axis. A schematic of the merger initialization is shown in Figure 2. Whenever projections of a simulation are taken, the viewing angle vector ($\boldsymbol{L}$) represents the position of the *observer* (i.e., the vector whose perpendicular plane is the projection plane). Each cluster is comprised of DM and star particles and gas defined on the grid distributed by choices of total mass, gas, and stellar profiles; all assumed to be spherically symmetric and in hydrostatic and virial

equilibrium. Any given deviation from these assumptions (e.g., triaxiality) would expand the parameter space beyond what is feasible for study, and furthermore, we expect deviations from spherical symmetry or hydrostatic equilibrium (HSE) to produce effects that are far subdominant relative to the primary merger-driven processes. We describe the overall setup in more detail below.

3.1.1. Total Mass Profiles

Each cluster component begins in HSE with the total mass following a truncated Navarro–Frenk–White (NFW) profile (Baltz et al. 2009):

$$\rho_{\rm tot}(r) \propto \frac{1}{(r/r_s)(1+r/r_s)^2}\left(\frac{1}{1+(r/r_t)^2}\right), \quad (1)$$

where $r_s = r_{200c}/c_{200c}$ is the scale radius and $r_t = 2r_{200c}$ is the truncation radius. For each cluster, the concentration parameter c_{200c} is computed with the `colossus` package (Diemer 2018), assuming a concentration−mass relation model from Diemer & Joyce (2019) for the cosmological parameters calculated in Planck Collaboration et al. (2020).

3.1.2. Gas Profiles

The gas density profiles follow a modified β-profile as given in Vikhlinin et al. (2006):

$$\rho_g(r) \propto \frac{(r/r_c)^{-\alpha/2}}{[1+(r/r_c)^2]^{3\beta/2-\alpha/4}} \cdot \frac{1}{[1+(r/r_s)^\gamma]^{\epsilon/(2\gamma)}}, \quad (2)$$

where r_c is the core radius, α is the inner slope parameter, β is the β-profile parameter, r_s is the scale radius ($>r_c$), γ controls the width of the outer transition, and ϵ is the outer logarithmic slope parameter. Here, we neglect the additional additive term introduced by Vikhlinin et al. (2006), which controls the inner core shape. The gas mass is normalized to the total mass within r_{500} through the assumed gas fraction from Sayers et al. (2019) based on the analysis of Mantz et al. (2010, $f_{\rm gas} = 0.115$). Assuming HSE and the total mass profile, this gas density profile uniquely determines the temperature, pressure, and entropy profiles.

In this work, we utilize three gas profiles that vary the degree of disturbedness of the gas in each galaxy cluster: strongly disturbed ("non-cool core"; NCC), moderately disturbed ("intermediate-cool core"; Int), and undisturbed ("cool core"; CC). The parameters for these profiles are given in Table 2. In the case of a simulation initialized with an undisturbed primary cluster gas profile and a secondary cluster gas profile that has been strongly disturbed, the total gas profile combination is notated CC+NCC, and the same logic applies for other combinations of gas profiles.

Analogs to the entropy profiles of these three gas distributions can be found in the observed profiles from galaxy clusters in the Archive of Chandra Cluster Entropy Profile Tables (ACCEPT; Cavagnolo et al. 2009) database. To illustrate this, in Figure 3, we plot the distribution of scaled best-fitting entropy profiles for 131 ACCEPT galaxy clusters at $z \geqslant 0.1$.

In order to minimize the effects of mass differences between the ACCEPT clusters and MACS J0018.5+1626, we utilize scalings between $K_{500} - T_{500}$ and $r_{500} - T_{500}$ to normalize the K and r axes of each calculated ACCEPT cluster entropy profile. We apply scalings derived from the self-similar model of Kaiser (1986) in the form outlined by Nagai et al. (2007), namely that

$$K_{500} \propto M_{500}^{2/3} \cdot E(z)^{-2/3}, \quad (3)$$

$$T_{500} \propto M_{500}^{2/3} \cdot E(z)^{2/3}, \quad (4)$$

and

$$M_{500} \propto r_{500}^3, \quad (5)$$

where $E(z)$ is the redshift scaling of the Hubble parameter.

We take the average cluster temperature reported by Cavagnolo et al. (2009) as an approximation of T_{500} for each ACCEPT cluster, and scale the K- and r-axes of each profile to $K_{\rm sc}$ and $r_{\rm sc}$ according to the above scalings as follows:

$$r_{\rm sc} = \frac{r}{(T_{\rm acc}/T_{\rm cl}) \cdot (E(z_{\rm cl})/E(z_{\rm acc}))^{4/3}}, \quad (6)$$

and

$$K_{\rm sc} = \frac{K(r)}{(T_{\rm acc}/T_{\rm cl})^{1/2} \cdot (E(z_{\rm cl})/E(z_{\rm acc}))^{1/3}}, \quad (7)$$

where $T_{\rm acc}$ is the average cluster temperature of the ACCEPT cluster being scaled, $T_{\rm cl}$ is the average cluster temperature of MACS J0018.5+1626 as reported in the ACCEPT database, and $E(z_{\rm cl})$ and $E(z_{\rm acc})$ are the relative expansion rates at the redshifts of MACS J0018.5+1626 and the relevant ACCEPT cluster, respectively. We further indicate the two populations identified by Cavagnolo et al. (2009) by plotting the mean best-

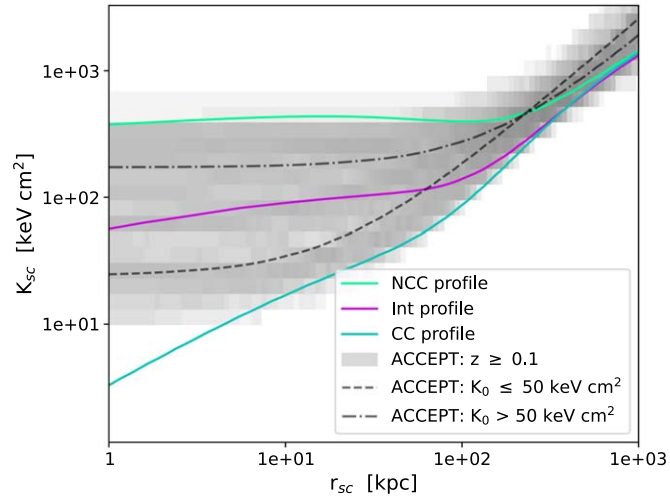

Figure 3. Scaled entropy distribution for ACCEPT galaxy clusters at $z \geqslant 0.1$. Simulated entropy profiles corresponding to our selection of initial gas profiles (NCC, Int, and CC) are overplotted. The simulated entropy profiles span the range of the observed distribution.

Table 2
Merger Simulation Gas Profile Parameters

Parameter	NCC Value	Int Value	CC Value
r_c [r_{2500}]	0.5	0.3	0.2
α	0.1	0.3	1.0
β	0.67	0.67	0.67
r_s [r_{200}]	1.1	1.1	1.1
γ	3.0	3.0	3.0
ϵ	3.0	3.0	3.0

fit entropy profiles for clusters with core entropy K_0 above and below 50 keV cm^2 scaled by the average $T_{\rm acc}$ and $E(z_{\rm acc})$ of each population. Figure 3 indicates that the NCC and CC entropy profiles are near the edges of the observed population, with Int approximately in the middle of the observed population.

With the gas profiles thus determined, the gas cells on the grid are assigned densities and pressures from these profiles, with their initial velocities set to zero in the rest frame of the cluster.

3.1.3. DM and Star Particle Initialization

Once we have both the gas mass and total mass profiles, the difference between these two yields the mass profile of DM and stars. In our simulations, these are represented by particles that interact between themselves and the gas only via gravity. DM and star particles are identical in our simulations, the latter being tagged as "star" type only to serve as a tracer of the center of each cluster as the merger evolves. This is done by setting the stellar mass profile as a truncated NFW profile (Equation (1)) with $\rho_{s,\ \rm star} = 0.9\rho_s$, $r_{s,\ \rm star} = 0.5 r_s$, and $r_{t,\ \rm star} = r_t$, which represents the large concentration of stars at the cluster potential minimum from the brightest cluster galaxy. To ensure that there is not a significant stellar contribution to the mass at large radii, we apply an exponential cutoff to the stellar profile at $r = 20$ kpc.

The particle positions and velocities are set up as discussed in previous works, most recently by Chadayammuri et al. (2022). For each of the particle positions, a random deviate $u = M(<r)/M_{\rm total}$ is uniformly sampled in the range [0, 1]. The mass profile $M(<r)$ for that particular mass type is inverted to give the radius of the particle from the center of the halo.

For the DM and star particles, their initial velocities are determined using the procedure outlined in Kazantzidis et al. (2004), where the energy distribution function is calculated via the Eddington formula (Eddington 1916):

$$\mathcal{F}(\mathcal{E}) = \frac{1}{\sqrt{8}\,\pi^2}\left[\int_0^{\mathcal{E}} \frac{d^2\rho}{d\Psi^2}\frac{d\Psi}{\sqrt{\mathcal{E}-\Psi}} + \frac{1}{\sqrt{\mathcal{E}}}\left(\frac{d\rho}{d\Psi}\right)_{\Psi=0}\right], \quad (8)$$

where $\Psi = -\Phi$ is the relative potential and $\mathcal{E} = \Psi - \frac{1}{2}v^2$ is the relative energy of the particle. We tabulate the function $\mathcal{F}$ in intervals of $\mathcal{E}$ to solve numerically for the distribution function at a given energy. Given the radius of the particle, particle speeds can then be chosen from this distribution function using the acceptance-rejection method. Once particle radii and speeds are determined, positions and velocities are determined by choosing isotropically distributed random unit vectors in $\mathfrak{R}^3$.

3.1.4. Epoch Readout

Once the mass profiles have been determined and the particles initialized, each galaxy cluster component is assigned an initial position and velocity, and data products are generated for a set of epochs as the merger evolves. We read out the simulations in increments of 0.02 Gyr, but only consider snapshots beginning 0.2 Gyr after the simulation initialization (defined as $t = 0$ Gyr) through $t = 2.1$ Gyr (well past the epoch of pericenter passage of a given merger).

For each merger simulation, the epoch at which pericenter passage occurs ($t_{\rm peri}$) is dependent on the initial conditions, most notably v_i. We, therefore, calculate $t_{\rm peri}$ as the epoch at which the distance between the positions of the primary and secondary halos is minimized, where the position of each halo is calculated simply as the median position of the star particles associated with the halo. For any simulation epoch t, $(t - t_{\rm peri})$ thus serves as an epoch proxy that can be compared from one simulation to another in a way that references time from the standard pericenter passage event, rather than the initial conditions.

3.2. Mock Observables

The best method of constraining galaxy cluster merger geometries from simulations is by comparing observational data to simulated observables (e.g., Springel & Farrar 2007; Lage & Farrar 2014; Chadayammuri et al. 2022). We derive mock observables from the merger simulations using the `yt` software (Turk et al. 2011) to project the XSB, total mass density, ICM density, kSZ effect amplitude, and galaxy velocities (using a subset of DM particles as proxies for the galaxies) into 2D images. For each mock observable, we use the MACS J0018.5+1626 redshift to determine the transformation from physical units to angular units in the sky. We then process these mock observables to make them nominally equivalent to the quality of the observational data. This consists of convolving the SZ-derived ICM projected density and LOS velocity maps with a 70″ FWHM Gaussian kernel, smoothing the XSB map to an effective resolution of 1.″96, convolving the projected total density map with a 1.″8 FWHM Gaussian kernel, and using the WVT and Beers et al. (1990) estimators described in Section 2.5 to bin the cluster-member galaxy velocities into a spatial map.

We use the `pyXSIM` package (ZuHone & Hallman 2016) to derive X-ray event files from the simulation data products in order to construct kT maps across the face of the cluster. We tailor the X-ray event files to include galaxy cluster emission, astrophysical foreground emission, and the Chandra/ACIS-I particle background by implementing the `SOXS instrument_simulator` tool (ZuHone et al. 2023). `pyXSIM` generates the simulated cluster emission using the cluster density, temperature, and velocity from the 3D simulations. In our case, we assume that the X-ray emission originates from an absorbed collisionally ionized plasma (`tbabs×apec`) with $n_{\rm H} = 4 \times 10^{20}$ cm^{-2}, at $z = 0.546$ (as in the MACS J0018.5+1626 observational data; see Section 2.2). As the simulation does not include metallicity, we assume $Z = 0.3\,Z_\odot$ throughout the cluster with Anders & Grevesse (1989) abundances. The 3D events are projected along a specified LOS and written to a 2D event file. In `SOXS`, we create a blank-sky background file by additionally writing the background/foreground events to a separate event file so that it can be subtracted in the same way as the observational blank sky background files in the X-ray temperature fitting (see Section 2.2). In this way, we construct simulated kT maps in an analogous way to the MACS J0018.5+1626 observables, following the observational spectral fitting methods within the same $r = 1.'8$ circular region.

4. Matching Simulations to Observations

In order to determine both the merger simulation initial conditions and the relevant observational parameters (e.g., the viewing angle of our LOS relative to the merger axis), which produce reasonable matches to the MACS J0018.5+1626

Table 3
Key Features in Each MACS J0018.5+1626 Observational Probe

Observable	Wavelength	Cluster Component	Features
ICM $v_{\rm pec}$	SZ + X-ray	LOS ICM velocity	∼E–W dipole with magnitude scale ∼4000–5000 km s^{-1} peak-to-peak (± ∼ 1000 km s^{-1})
$v_{\rm gal}$	Optical ($z_{\rm spec}$)	LOS DM velocity	∼NW–SE dipole with magnitude scale ∼3000 km s^{-1} peak-to-peak
XSB	X-ray	POS ICM morphology	Extended/diffuse emission elongated along the NE–SW axis
			Lacking two well-separated emission peaks
kT	X-ray	POS ICM morphology	Hot, centrally peaked temperature distribution elongated along NE–SW axis with maximum cell at ∼15 keV
			Lacking two well-separated cool cores
τ	SZ + X-ray	POS ICM morphology	Centrally peaked distribution with tail extending NE
Σ	Optical (GL)	POS DM morphology	Two centrally located mass peaks separated by ∼22″ along the NE–SW axis

observational data, we apply a set of matching criteria to mock observables generated with a wide range of simulation parameters (described in Section 4.6). The matching criteria we apply to the resulting mocks are designed to select key features from the MACS J0018.5+1626 observables, so that physical information (e.g., the merger epoch or viewing angles) can be determined. We manually calibrate these matching criteria on each MACS J0018.5+1626 cluster observable, with the exception of the ICM $v_{\rm pec}$ map. In this case, the low S/N of the ICM $v_{\rm pec}$ map prevented us from identifying a categorical matching criterion, and we, therefore, developed a more formal statistical comparison for this observable (see Section 4.1 below). The key features of each observational probe are summarized in Table 3, and the associated matching criteria are described in the following sections.

4.1. ICM v_{pec} Map

The MACS J0018.5+1626 kSZ-derived ICM $v_{\rm pec}$ map morphologically resembles an approximately east–west (E–W) dipole with a velocity difference of ∼4000–5000 km s^{-1} peak-to-peak (though the uncertainties in this map are significant at ∼1000 km s^{-1}). In order to maximally utilize the MACS J0018.5+1626 ICM $v_{\rm pec}$ information to place constraints on the simulated ICM $v_{\rm pec}$ maps while taking these substantial observational uncertainties into account, we apply the following method.

We begin by generating 1000 noise realizations ($N_{\rm X}$) of the MACS J0018.5+1626 observational ICM $v_{\rm pec}$ map ($M_{\rm obs}$). These realizations fully capture all of the noise fluctuations, including correlations, due to both the instrument and residual astrophysical contamination. In brief, the single-band noise realizations described in Sayers et al. (2019) are created for both the 140 and 270 GHz SZ images. These include jackknife images to estimate noise due to the instrument and atmosphere, along with random realizations of primary CMB fluctuations and the relevant galaxy populations (dusty star-forming and radio active galactic nuclei). We then obtain a $v_{\rm pec}$ map for each of these realizations (i.e., the $N_{\rm X}$) using the same procedure applied to the observed data. Finally, we compute the rms of the 1000 realizations within each pixel to obtain $M_{\rm RMS}$, which is a map that provides the positionally dependent uncertainty per pixel. While $M_{\rm RMS}$ is not a complete description of the noise due to pixel–pixel correlations, it can be used as a proxy to estimate the goodness of fit, as detailed below.

For each simulated ICM $v_{\rm pec}$ map ($M_{\rm sim}$), we begin by binning $M_{\rm sim}$ to an identical pixel scale as $M_{\rm obs}$ and trim both maps to a circular region of $r = 3'$ centered on MACS J0018.5+1626 for consistency between the maps. For each $N_{\rm X}$, we generate a noisy simulated map $M_{\rm noisy} = (M_{\rm sim} + N_{\rm X}) - w$, where w represents the uncertainty weighted mean of $(M_{\rm sim} + N_{\rm X})$. The value of w is similarly calculated and subtracted from the observed map $M_{\rm obs}$ in order to remove the overall bulk velocity of the system. This procedure gives us 1000 noisy simulated maps, from which we empirically determine a simulated χ^2 distribution defined by the statistic:

$$\chi^2_{\rm sim} = \sum_i \frac{(M_{{\rm noisy},i} - M_{{\rm sim},i})^2}{(M_{{\rm RMS},i})^2}, \tag{9}$$

for i pixels in each map.

We then define for each $M_{\rm sim}$ an observational $\chi^2_{\rm obs}$ assuming $M_{\rm sim}$ is the true underlying velocity distribution:

$$\chi^2_{\rm obs} = \sum_i \frac{(M_{{\rm obs},i} - M_{{\rm sim},i})^2}{(M_{{\rm RMS},i})^2}, \tag{10}$$

for i pixels in each map. Next, we use the empirically determined distribution of $\chi^2_{\rm sim}$ values to identify the benchmark where the probability-to-exceed (PTE; often referred to as a p-value) of the $\chi^2_{\rm sim}$ distribution is 0.30. Our matching criterion, therefore, requires that PTE > 0.30 for a given $\chi^2_{\rm obs}$. In Figure 4, we plot examples of simulated ICM $v_{\rm pec}$ maps, one of which passes the matching criterion (i.e., PTE > 0.30 for the corresponding value of $\chi^2_{\rm obs}$), and one of which fails (PTE < 0.30 for $\chi^2_{\rm obs}$).

4.2. GL Mass Reconstruction Map

The MACS J0018.5+1626 GL mass reconstruction map reveals two centrally located mass peaks separated by ∼22″ (≃140 kpc at $z = 0.546$) along the northeast–southwest (NE–SW) axis. We associate these peaks with the centers of the mass distributions of the primary and secondary cluster components in the merger. In order to reproduce this morphology, we require simulation snapshots to exhibit primary and secondary cluster mass peaks separated by ±50% of this observational angular separation ($11'' \leqslant \theta_{\rm GL} \leqslant 33''$).

4.3. XSB Map

The MACS J0018.5+1626 XSB map indicates the presence of extended X-ray emission elongated along the NE–SW axis. Unlike the GL mass map, this emission lacks two clearly identifiable peaks, so from our viewing angle, the gas appears as a single-peaked distribution. This implies that the merger has progressed to a point where significant interactions between the gas in the original systems have already occurred. To select for

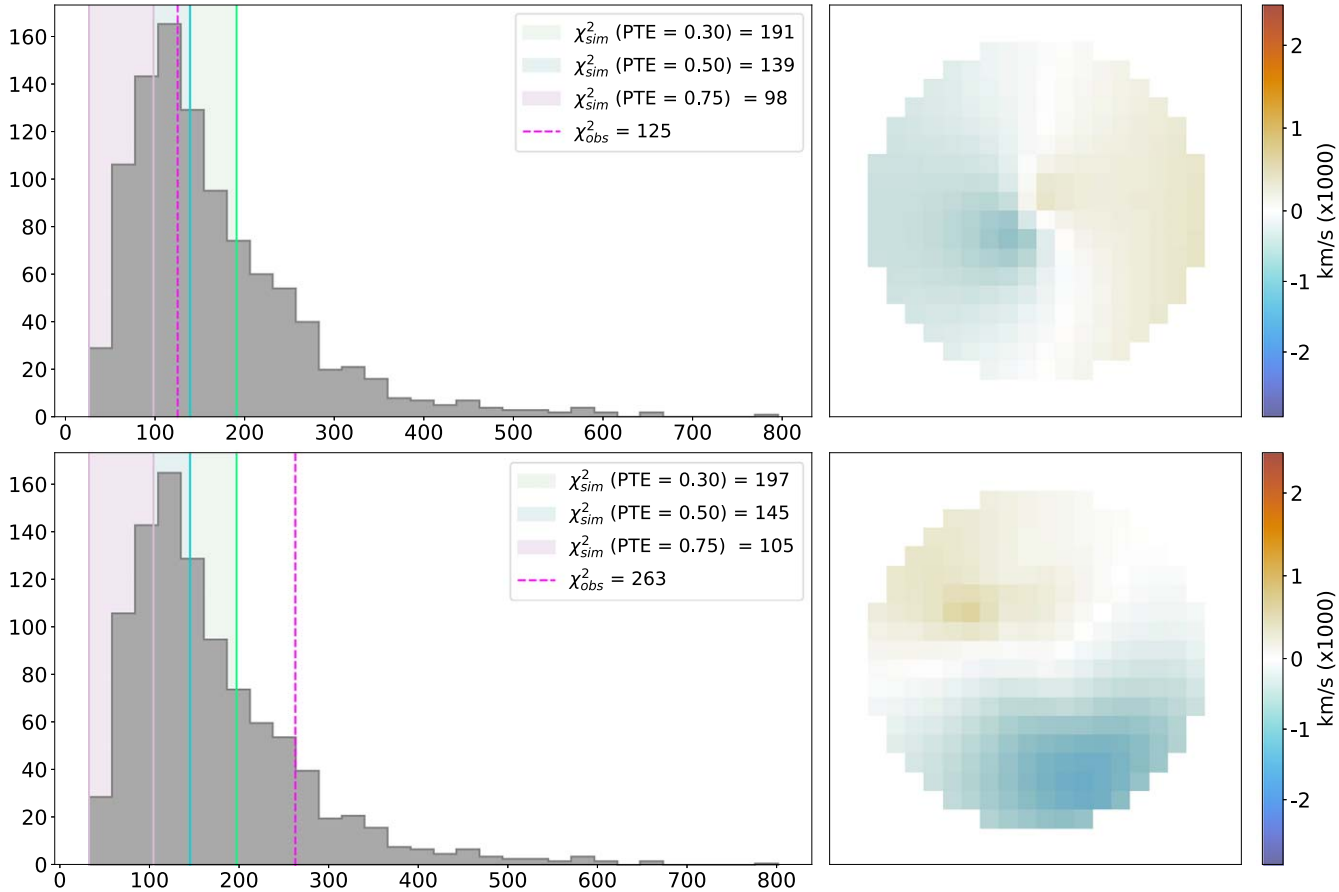

Figure 4. Top: simulated ICM $v_{\rm pec}$ map and empirically determined distribution of $\chi^2_{\rm sim}$ values with $\chi^2_{\rm obs}$ indicated for a simulation with $R = 1.5$, $b = 250$ kpc, $v_i = 3000$ km s^{-1}, gas profile: Int+NCC, and $|\boldsymbol{L} \cdot \hat{x}| = 0.88$ at an epoch 0.06 Gyr after pericenter passage. This mock ICM $v_{\rm pec}$ passes the matching criterion. Bottom: same, at an epoch 1 Gyr after pericenter passage. This mock ICM $v_{\rm pec}$ map fails the matching criterion. In each figure, the shaded regions associated with each PTE threshold represent the range of $\chi^2_{\rm obs}$ values that would be allowed by the threshold.

this quality, we exclude simulation snapshots wherein we identify two distinct intensity peaks (with `peak_local_max` from `scikit-image`; van der Walt et al. 2014) separated by $>3''$ ($\simeq$20 kpc at $z = 0.546$).

4.4. kT *Map*

The MACS J0018.5+1626 X-ray derived kT map indicates a hot ($kT_{\rm max} \sim 15$ keV), centrally peaked temperature distribution elongated along the NE–SW axis. The kT map lacks any evidence for an intact cool core, indicating that either the original gas distributions have already been significantly impacted by the merger, or that neither cluster initially possessed a cool core. We, therefore, employ two matching criteria to the simulated kT maps. First, in order to exclude snapshots where the temperature distribution is globally much higher than that of MACS J0018.5+1626, we require simulation snapshots to have a median temperature across the kT map of <15 keV. Second, to identify simulation snapshots that exhibit a centrally peaked temperature distribution, we require that simulated kT maps have $kT > 9.5$ keV plasma in every cell within a central map region defined by a circle with $r = 20''$. These two criteria jointly exclude simulated snapshots which exhibit clear cool cores and/or global temperatures inconsistent with the MACS J0018.5+1626 kT map.

4.5. v_{gal} *Map*

The MACS J0018.5+1626 $z_{\rm spec}$-derived $v_{\rm gal}$ map morphologically resembles a ~NW–SE dipole with magnitude scale $\Delta v_{\rm gal,\ obs} \approx 3100$ km s^{-1} peak-to-peak. In order to identify simulation snapshots where the galaxy velocities replicate this dipole magnitude, we require that the absolute magnitude difference across the simulated $v_{\rm gal}$ maps ($\Delta v_{\rm gal,\ sim}$) be within the 1σ statistical uncertainty (± 940 km s^{-1}) of the MACS J0018.5+1626 $v_{\rm gal}$ absolute magnitude difference. This enforces the criterion $\Delta v_{\rm gal,\ sim} = 3100 \pm 940$ km s^{-1}.

In addition, the MACS J0018.5+1626 observables reveal a rotational offset in projection between the LOS ICM and DM velocity dipoles (by way of the ICM $v_{\rm pec}$ and $v_{\rm gal}$ maps), which we attribute to the decoupling of the DM and gas velocities during the merger. In order to identify simulation snapshots that similarly exhibit a projected rotation between the ICM $v_{\rm pec}$ and $v_{\rm gal}$ maps, we first fit a 2D first-degree polynomial to each of the observationally derived MACS J0018.5+1626 ICM $v_{\rm pec}$ and $v_{\rm gal}$ maps with `lmfit`. Using these models, we identify for each observable the axis on which the velocity extrema lie (i.e., the vector that goes through the median positions of the 10% highest and lowest velocity values in the best-fit model map). Then, we calculate the absolute value of the angular offset between the axes of velocity extrema in the ICM $v_{\rm pec}$ and $v_{\rm gal}$ maps. The resulting MACS J0018.5+1626 $\Delta\theta_{v,\rm obs}$ is $\approx 135°$. We then apply the same formalism to the simulated ICM $v_{\rm pec}$

Table 4
Merger Simulation Parameter Space Sampled in the First Application of the Matching Criteria to Determine the Primary and Secondary Cluster Gas Profiles

Parameter	Value(s)
Fixed	
R	1.5
b	250 kpc
v_i	3000 km s^{-1}
Epoch	{0.20, 0.22, 0.24, 0.26,...,2.10} Gyr
$\lvert \boldsymbol{L} \cdot \hat{x} \rvert$	{0.65, 0.69, 0.73,...,1}
Varied	
Gas profile	NCC+CC, NCC+Int, NCC+NCC, Int+CC, Int+Int, Int+NCC

and $v_{\rm gal}$ maps for each simulated snapshot and require that $\Delta\theta_{v,\rm sim}$ is within 45° of $\Delta\theta_{v,\rm obs}$. This excludes simulated snapshots where the ICM and DM velocities are either fully coupled or are decoupled in a manner that is inconsistent with the MACS J0018.5+1626 observables.

4.6. Applications of the Matching Criteria

In order to constrain the primary and secondary cluster gas profiles, we first generated a set of simulations with reasonable initial guesses for R, b, and v_i while individually varying the primary and secondary cluster gas profiles (see Table 4). We sample the simulations at the epochs defined in Section 3.1.4 over a grid of $\boldsymbol{L}$ vectors. Here, $\boldsymbol{L}$ is defined by a set of vectors spaced evenly in $\lvert \boldsymbol{L} \cdot \hat{x} \rvert$ space with randomly populated $(\hat{y}, \hat{z})$ components.

The simulations are initialized with combinations of gas profiles assigned to the primary and secondary cluster components (see Section 3.1.2). We sample simulations where the primary cluster gas profile has been either moderately or strongly disturbed (by, e.g., recent merger activity) and the secondary cluster gas profile is any one of undisturbed, moderately, or strongly disturbed. We do not include simulations where the primary cluster gas profile is undisturbed in this suite due to the lack of evidence in the MACS J0018.5+1626 observables for a strong cool core in the X-ray-derived observables.

When consolidated into a single matching algorithm and applied to the simulations, this first application of the matching criteria reduces the simulated parameter space to 107 out of 4.4×10^4 snapshots (0.2%). In Figure 5, we plot weighted distributions of gas profiles, epochs, and viewing angles associated with the simulation snapshots that pass the application of the matching criteria. In order to account for biases on mock observable evolution rates that different initial conditions can produce (e.g., simulations initialized with higher v_i will be sampled less finely in space relative to those initialized with lower v_i due to the fixed epoch readout increment), each snapshot's contributions to the distributions are weighted by the relative velocity of the cluster component cores at that snapshot. The cluster relative velocities are calculated using the median velocity of the star particles associated with each halo. From this weighted gas profile distribution, we select the Int+NCC combination as the profile that best fits the observational data given our fixed initial conditions. We reserve a full discussion of the gas profile variation matching results for Section 5.1, and choose to fix the Int+NCC gas profiles for further simulation runs.

Next, in order to constrain R, b, and v_i for the MACS J0018.5+1626 system, we generated a set of simulations with Int+NCC gas profiles, while individually varying R, b, and v_i (see Table 5). The epoch and viewing angle sampling is identical to the first set of simulations described above. We then performed a second application of the matching criteria to this set of simulations, which reduces the simulated parameter space to 432 out of 1×10^5 snapshots (0.4%). We illustrate and interpret the resulting weighted distributions of R, b, v_i, epochs, and viewing angles that pass the matching criteria in Section 5.

5. Parameter Variation Results

In the following sections, we describe the results of the first and second applications of the matching criteria (see Section 4.6) to our simulation suite for each of the initial conditions that were varied in the simulation initializations (gas profiles, mass ratio, impact parameter, and initial relative velocity), in addition to key observable parameters (epoch and viewing angle). As described in Section 4.6, we individually vary one initial parameter for each simulation rather than marginalizing over all correlations between merger parameters (with, e.g., an MCMC) due to computational limitations. We, therefore, do not expect the resulting weighted parameter distributions to be exactly equivalent to rigorously determined posterior probability distributions, which would allow us to compute formal confidence limits on each parameter. Instead, when reporting ranges of parameters consistent with the MACS J0018.5+1626 observables, we identify for each initial parameter any value that produces a set of snapshots greater than 50% as likely as the most likely sampled value determined by the weighted distributions resulting from the matching criteria applications.

5.1. Gas Profiles

In the first application of the matching criteria to the simulations with varying gas profiles, simulations with either a moderately or strongly disturbed secondary gas profile are strongly preferred to those with an undisturbed secondary gas profile. No simulation with an undisturbed secondary gas profile produces any snapshots that pass the matching criteria. This is sensible since there are no clear indicators of a prominent cool core in any of the MACS J0018.5+1626 observables with which the matching criteria are empirically calibrated. We note that the cool core can be destroyed as a result of the merger, although the initial conditions and epochs associated with this scenario are excluded by our matching criteria.

In addition, simulations with a moderately disturbed primary gas profile are preferred to those with a strongly disturbed gas profile. We find that simulations that utilize a strongly disturbed primary gas profile generally produce mock observables that are more extreme than the MACS J0018.5+1626 observables. For example, the resulting simulated kT maps are much hotter ($kT_{\rm max} \gtrsim 20$ keV) at epochs near pericenter passage than the MACS J0018.5+1626 kT map. There exists a moderate preference for a strongly disturbed secondary gas profile that is evident both when the primary gas profile is moderately disturbed and when it is strongly disturbed. The only simulation initialized with gas profiles other than

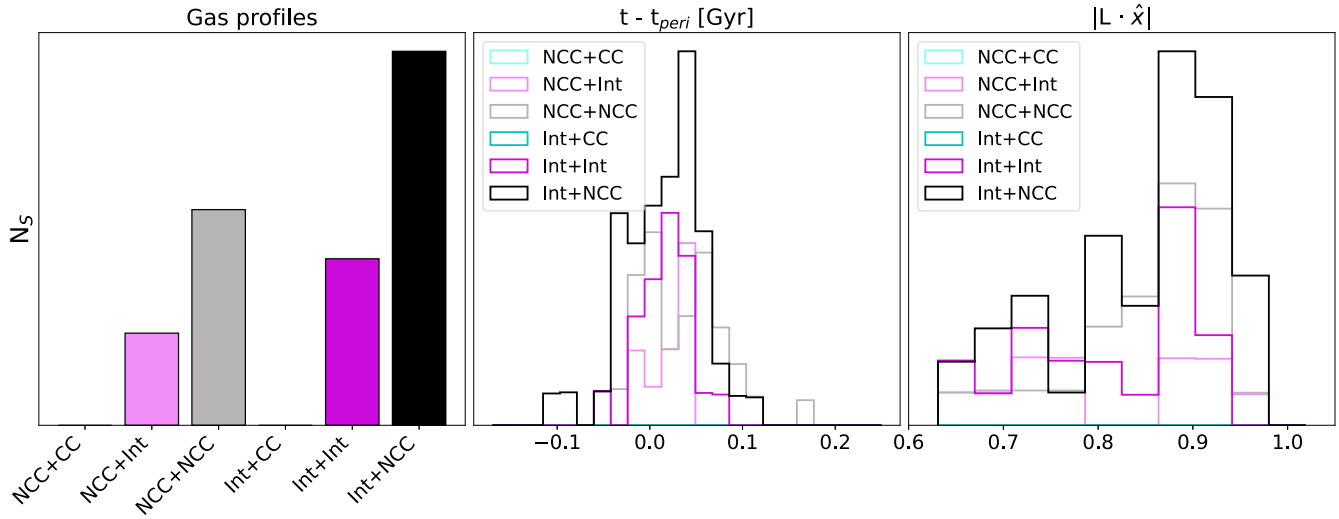

Figure 5. Weighted distribution of gas profiles, epochs, and viewing angles for simulated snapshots with $R = 1.5$, $b = 250$ kpc, $v_i = 3000$ km s^{-1} that pass the matching criteria. The Int+NCC gas profile combination is preferred by the matching algorithm. The epoch distribution peaks slightly after the pericenter passage, and viewing angles offset from the merger axis by ≈20°–30° are most strongly preferred.

Table 5
Merger Simulation Parameter Space Sampled in the Second Application of the Matching Criteria to Determine the Epoch, Viewing Angle, R, b, and v_i Based on the Gas Profile Results from the First Application of the Matching Criteria

Parameter	Value(s)
	Fixed
Gas profile	Int+NCC
Epoch	{0.20, 0.22, 0.24, 0.26,...,2.10} Gyr
$\lvert \boldsymbol{L} \cdot \hat{x} \rvert$	{0.65, 0.69, 0.73,...,1}
	Varied
R	{1.2, 1.5, 2.0, 3.0, 5.0}
b	{0, 50, 100, 250, 500} kpc
v_i	{1000, 1700, 2400, 3000, 3800, 5000} km s^{-1}

Int+NCC that produces snapshots greater than 50% as likely as the most likely sampled gas profile combination (Int+NCC) is that with an NCC+NCC gas profile (only ≃58% as likely). Based on these preferences from the first matching criteria application, we select the Int+NCC gas profile combination for use in the simulations wherein R, b, and v_i are varied.

5.2. Merger Epoch

In both the first application of the matching criteria to the simulations with varying gas profiles and the second application to the simulations with varying R, b, and v_i, there is a strong selection for simulation snapshots within −0.1 (0.2) Gyr before (after) the calculated epoch of pericenter passage in each merger simulation. We plot the weighted distribution of selected epochs for simulation snapshots that pass the matching criteria for all the simulation variations described above in Figure 6. The distribution rises with a roughly Gaussian shape beginning at ≈0.1 Gyr before the pericenter passage, peaks at $t - t_{\rm peri} \approx 0.03$ Gyr, then falls off similarly in a roughly Gaussian shape within ≈0.1 Gyr of the pericenter passage, before a later-time wing takes over and falls to zero at $t - t_{\rm peri} \approx 0.2$ Gyr. Quantitatively, the median of selected epochs is 0.03 Gyr after the pericenter passage with an interquartile range (IQR) of 0.06 Gyr. The MACS J0018.5+1626

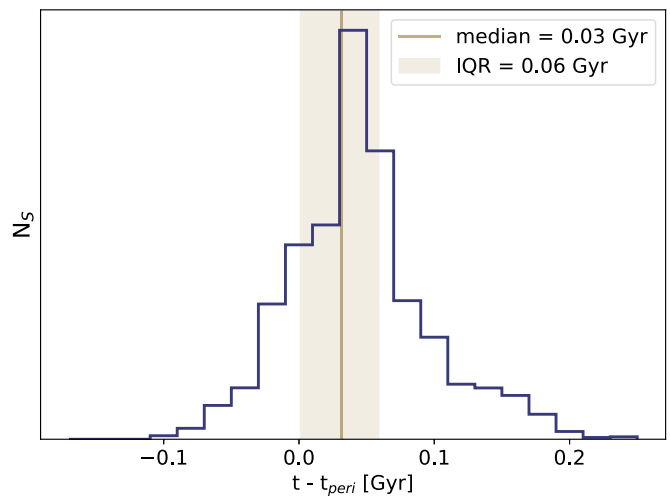

Figure 6. Weighted distribution of epochs for simulation snapshots that pass the matching criteria. The outputs of both applications of the matching criteria are used to generate the full weighted epoch distribution here. The median of selected epochs is 0.03 Gyr after the pericenter passage, with an IQR of 0.06 Gyr.

merger epoch $t - t_{\rm peri}$ is, therefore, likely in the range of 0–60 Myr after the pericenter passage.

To further illustrate this result, we plot the evolution of mock maps at $t - t_{\rm peri} = -0.3$, −0.1, 0, 0.1, and 0.3 Gyr for a simulation with initial conditions and observational parameters that are reasonably favored by the matching algorithm in Figure 7. In each panel, we indicate whether the observable passes its corresponding matching criterion with a green check mark (pass) or a red X (fail). In the XSB observable progression, the clearly identifiable emission peaks associated with each cluster are disrupted, and the maps become more spatially extended as the merger evolves beyond the pericenter passage. Only XSB maps after the pericenter passage epoch pass the XSB matching criterion. The kT progression indicates that the global temperature rapidly increases around the pericenter passage of the clusters when central regions of gas are heated by merger-driven shocks, and cools globally shortly thereafter. Only snapshots from the pericenter passage to

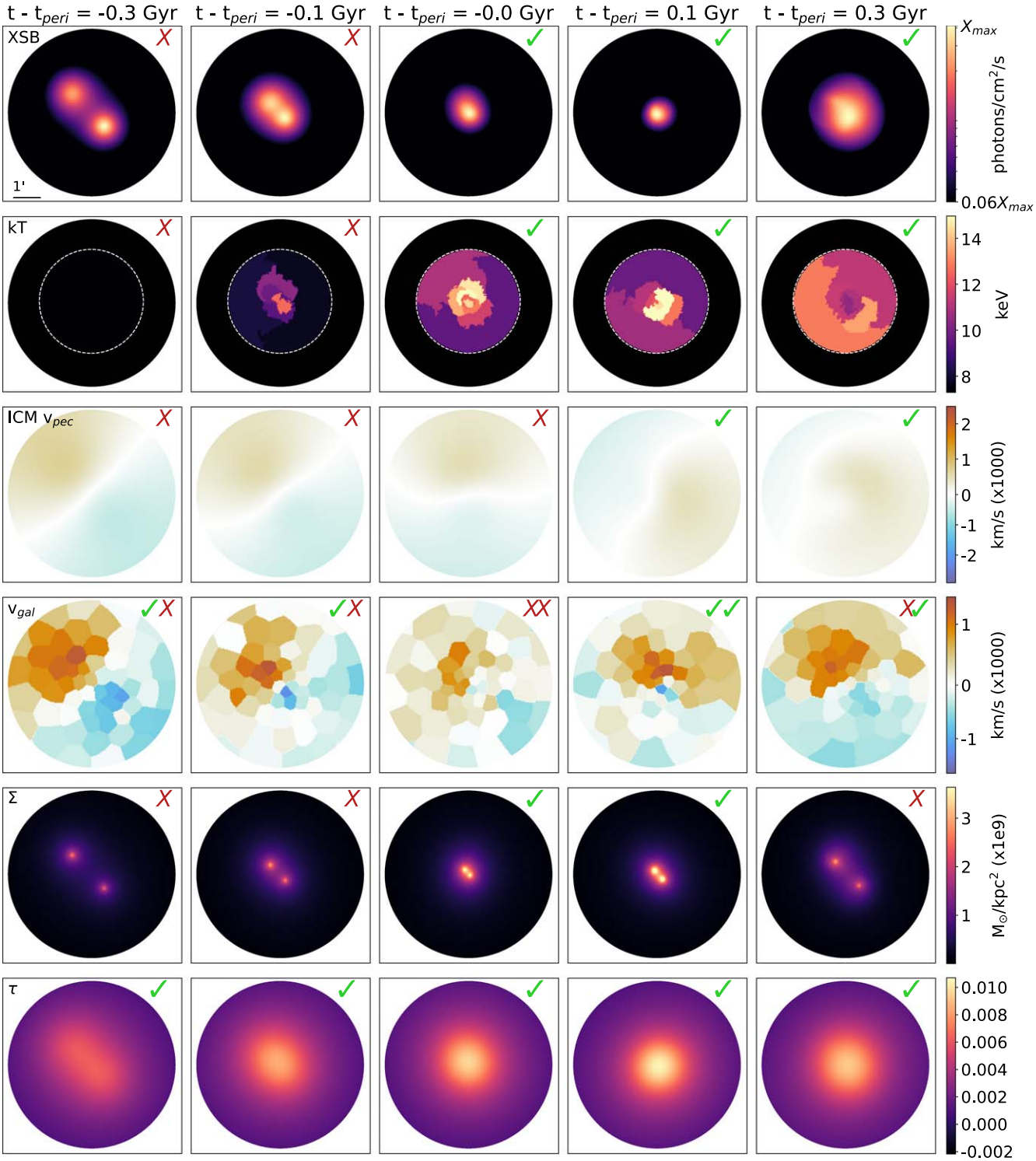

Figure 7. Evolution of mock observables as a function of epoch with indicators for the pass/fail status of each mock observable to the corresponding matching criterion. Row 1: XSB evolution. The 99th percentile in XSB ($X_{\rm max}$) sets the upper bound of the color bar, while the lower bound is fixed in order to span the same relative flux scale as the MACS J0018.5+1626 XSB map. Row 2: kT evolution. Row 3: ICM $v_{\rm pec}$ evolution. Row 4: $v_{\rm gal}$ evolution. The leftmost indicator in each panel represents the pass/fail status of the $\Delta v_{\rm gal,\ sim}$ magnitude matching criterion. The rightmost indicator represents the pass/fail status of the $\Delta\theta_{v,\rm sim}$ rotational offset with the ICM $v_{\rm pec}$ map. Row 5: Σ evolution. Row 6: τ evolution. Note that we do not apply an individual matching criterion to mock τ maps due to the minimal constraining power of the MACS J0018.5+1626 τ map. The only simulation snapshot shown here that passes all of the matching criteria is at $t - t_{\rm peri} \approx 0.1$ Gyr (i.e., column 4).

$t - t_{\rm peri} = 0.3$ Gyr pass the temperature matching criteria for this simulation. In the ICM $v_{\rm pec}$ observable progression, the ICM velocity dipole structure is highly disrupted around the pericenter passage, after which it rotates in the POS relative to the $v_{\rm gal}$ dipole. Only snapshots after the pericenter passage epoch, when the dipole orientation matches that of MACS J0018.5+1626, are selected by the ICM $v_{\rm pec}$ matching criterion. The $v_{\rm gal}$ progression shows a high galaxy velocity

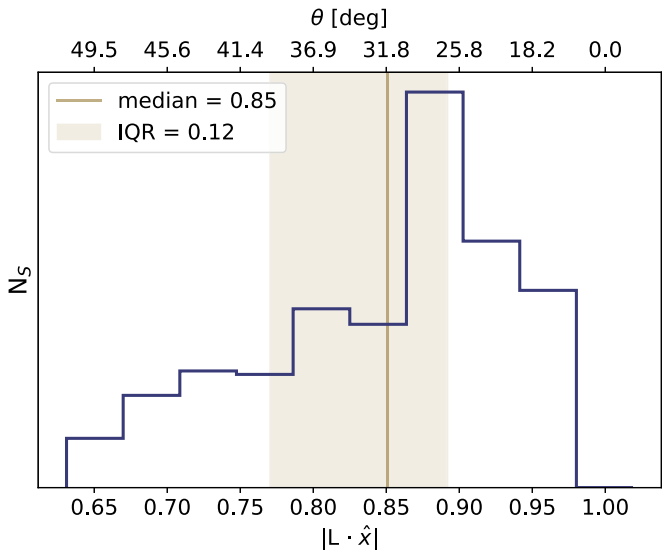

Figure 8. Weighted distribution of viewing angles for simulation snapshots that pass the matching criteria. As in Figure 6, the outputs of both applications of the matching criteria are used to generate the full weighted viewing angle distribution here. The median of the selected viewing angles is $|\boldsymbol{L} \cdot \hat{x}| = 0.85$ ($\approx 32°$) with an IQR of 0.12 ($\approx 13°$).

magnitude difference at early epochs that is reduced at pericenter passage as the DM halos pass the point of their closest approach (projected along the LOS). All snapshots prior to the pericenter passage epoch are therefore selected by the $v_{\rm gal}$ matching criterion, in addition to one snapshot immediately after the pericenter passage at $t - t_{\rm peri} = 0.1$ Gyr. The rotational offset between the ICM $v_{\rm pec}$ and $v_{\rm gal}$ dipoles is only of sufficient magnitude to pass the $\Delta\theta_{v,\rm sim}$ matching criterion at epochs after pericenter passage, meaning that the only snapshot shown that passes all three velocity criteria is at $t - t_{\rm peri} = 0.1$ Gyr. In the Σ observable progression, snapshots from the pericenter passage epoch until $t - t_{\rm peri} = 0.1$ Gyr produce total projected mass peaks that are separated within the bounds set by the matching criteria. Finally, the τ progression is shown for reference. We do not apply any matching criteria to the τ map, since any reasonable choice of input parameters yields τ maps that are consistent with the MACS J0018.5+1626 τ map, given the large observational uncertainties.

These evolutionary trends validate the result of the matching algorithm applications, i.e., that the mock observables favor a merger occurring near or shortly after pericenter passage. For a simulation with $R = 1.5$, $b = 250$ kpc, $v_i = 1700$ km s^{-1}, gas profile: Int+NCC, and $|\boldsymbol{L} \cdot \hat{x}| = 0.84$, the snapshots which pass the matching criteria are at $t - t_{\rm peri} = 0.04$, 0.06, and 0.08 Gyr. In Figure A1, we show an animation of the evolution of mock observables as a function of epoch for a simulation with $R = 1.5$, $b = 250$ kpc, $v_i = 1700$ km s^{-1}, gas profile: Int+NCC, and $|\boldsymbol{L} \cdot \hat{x}| = 0.92$.

5.3. Viewing Angle

In both the first and second applications of the matching criteria to the simulations, there is a strong selection of simulation snapshots observed at viewing angles marginally offset from the merger axis. We plot the weighted distribution of selected viewing angles for simulation snapshots that pass the matching criteria for all the simulation variations in Figure 8. In particular, the matching algorithm prefers values of $|\boldsymbol{L} \cdot \hat{x}|$ that peak at ≈ 0.88 (i.e., inclined $\approx 28°$ from the merger axis). Quantitatively, the median of the selected viewing angles is $|\boldsymbol{L} \cdot \hat{x}| = 0.85$ ($\approx 32°$) with an IQR of 0.12 ($\approx 13°$). The MACS J0018.5+1626 viewing angle is, therefore, likely between $0.77 \lesssim |\boldsymbol{L} \cdot \hat{x}| \lesssim 0.89$ (inclined $\approx 27°$–$40°$). In no case does a merger oriented along the line of sight ($|\boldsymbol{L} \cdot \hat{x}| = 1$) pass the matching criteria.

Furthermore, the degree of decoupling in the POS between the gas and DM velocity dipole structures, as traced by the ICM $v_{\rm pec}$ and $v_{\rm gal}$ maps, varies strongly as a function of the viewing angle. We describe these dependencies in detail in Section 6.

5.4. Mass Ratio

The mass ratio is similarly constrained in the second application of the matching criteria, assuming a fixed gas profile, b, and v_i. The resulting weighted distribution of R values selected by the matching algorithm is shown in Figure 9. While the distribution peaks at $R = 1.5$, simulations initialized with mass ratios of $R = 2.0$ and 3.0 are greater than 50% as likely as those with $R = 1.5$. The likelihood of reproducing the data falls off rapidly (less than 50% as likely as the most likely sampled mass ratio) for larger and smaller mass ratios ($R = 1.2$ and 5.0), which indicates that the mass ratio of MACS J0018.5+1626 is likely between $R \approx 1.5$ and 3.0.

5.5. Impact Parameter

The MACS J0018.5+1626 impact parameter is constrained in the second application of the matching criteria, assuming a fixed gas profile, R, and v_i. The resulting weighted distribution of b values selected by the matching algorithm is shown in Figure 9. The distribution formally peaks at $b \approx 250$ kpc, and the likelihood of reproducing the data falls off sharply for $b > 250$ kpc. However, all sampled impact parameters less than this value, while less likely, are still plausible (greater than 50% as likely as $b \approx 250$). We, therefore, place an upper limit on the MACS J0018.5+1626 impact parameter of $b \lesssim 250$ kpc. At the epoch of pericenter passage, the separation between the cluster cores (i.e., the pericenter distance) is $\simeq 90$ kpc for a simulation initialized with $R = 1.5$, $b = 250$ kpc, $v_i = 1700$ km s^{-1}, and gas profile: Int+NCC.

However, we note that this impact parameter constraint is highly dependent on the degree of observed rotational offset between the ICM $v_{\rm pec}$ and $v_{\rm gal}$ maps. In Section 6, we illustrate the dependencies of the constrained impact parameter on the velocity decoupling.

5.6. Initial Relative Velocity

The initial relative velocity of the MACS J0018.5+1626 cluster components is similarly constrained in the second application of the matching criteria, assuming a fixed gas profile, b, and R. The resulting weighted distribution of v_i values selected by the matching algorithm is shown in Figure 9. The distribution peaks at $v_i \approx 2400$–3000 km s^{-1}. The most likely initial relative velocity based on the weighted distribution is $v_i = 2400$ km s^{-1}, but simulations initialized with initial relative velocities of $v_i = 3000$ and 1700 km s^{-1} are greater than 50% as likely as those with $v_i = 2400$ km s^{-1}. Initial relative velocities of $v_i = 1000$, 3800, and 5000 km s^{-1} produce snapshots less than 50% as likely as the most likely sampled initial relative velocity. We, therefore, conclude that MACS

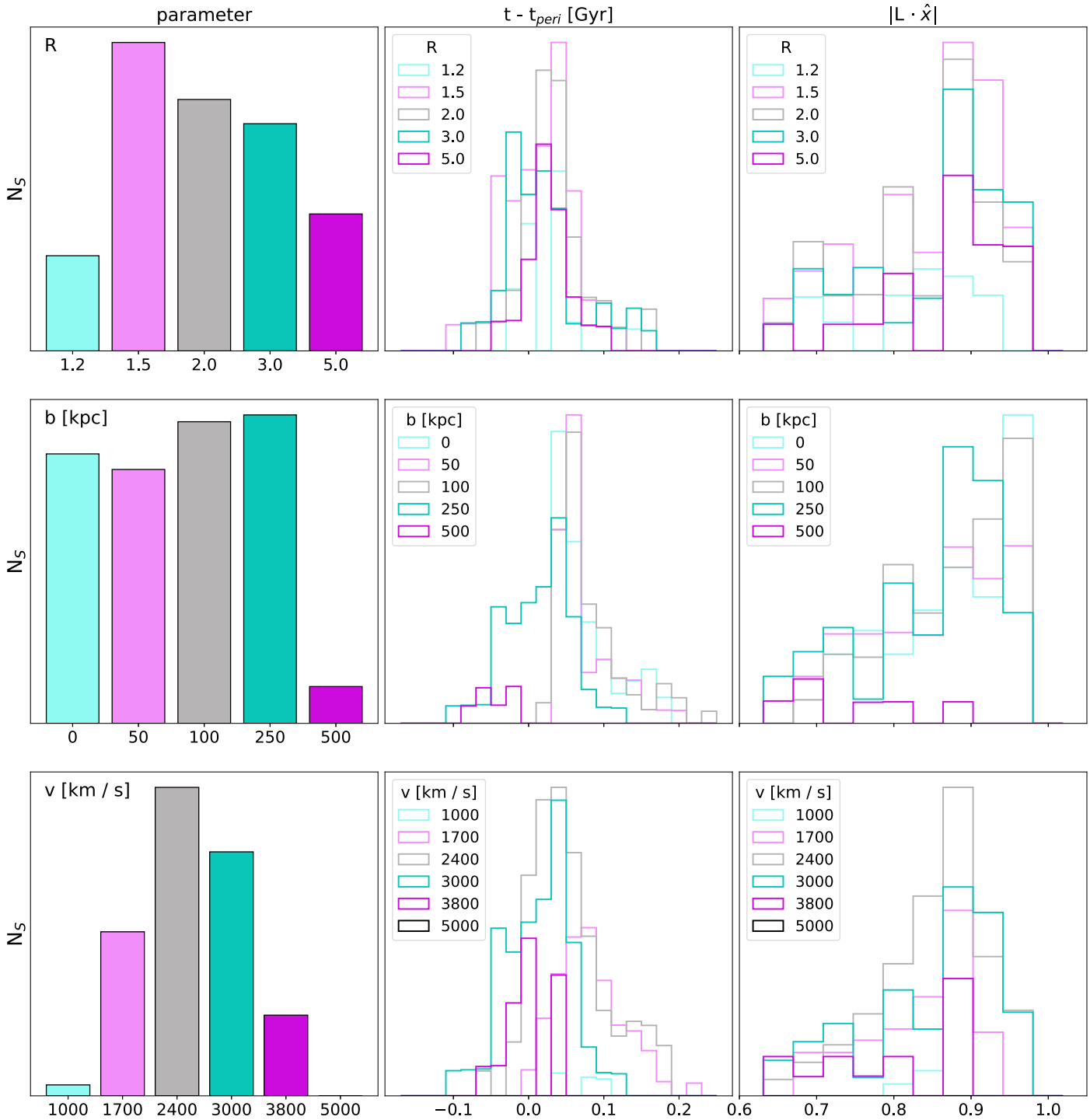

Figure 9. Weighted distributions of varied parameters (top: mass ratio, middle: impact parameter, bottom: initial relative velocity), epochs, and viewing angles from simulated snapshots that pass the matching criteria. The default parameters that are held fixed unless explicitly varied are $R = 1.5$, $b = 250$ kpc, $v_i = 3000$ km s^{-1}, and gas profile: Int+NCC. Impact parameters of $b \lesssim 250$ kpc, mass ratios of $R \approx 1.5$–3.0, and initial relative velocities of $v_i \approx 1700$–3000 km s^{-1}, are preferred by the matching criteria. The weighted epoch distributions peak around or shortly after the pericenter passage, and viewing angles offset from the merger axis by $\approx 15°$–35° are preferred by the matching criteria.

J0018.5+1626 likely has an initial relative velocity between $v_i \approx 1700$ and 3000 km s^{-1}.

Using a suite of N-body simulations in a ΛCDM cosmology, Li et al. (2020) constructed a distribution of the velocity (v) of infalling subhalos as a function of mass and redshift. They found a nearly universal log-normal distribution that peaks near the virial velocity (V_h) of the primary subhalo ($v/V_h \approx 1.15$). For a primary subhalo at the mass and redshift of MACS J0018.5+1626 assuming a mass ratio of $R \approx 1.5$, the Li et al. (2020) subhalo infall velocity distribution has a median velocity of $\approx$1800 km s^{-1} with a 2σ range from $\approx$1200–2600 km s^{-1} (see Figure 10). It is important to note that the underlying cause of the spread of initial velocities in our analysis is measurement uncertainty, while for the Li et al. (2020) analysis, it is due to

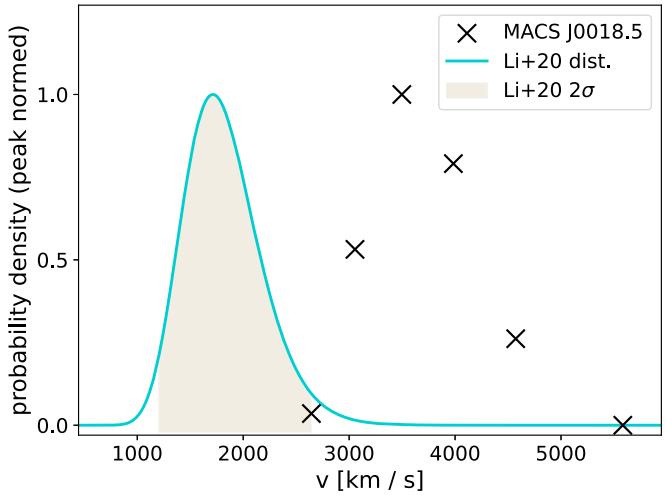

Figure 10. Comparison of the calculated MACS J0018.5+1626 infall velocity weighted distribution (Figure 9) to the subhalo infall velocity distribution from Li et al. (2020). All values have been peak-normalized for straightforward comparison. The MACS J0018.5+1626 velocities indicate that MACS J0018.5 +1626 is a relatively exceptional object compared to those studied by Li et al. (2020).

cosmic variance. Thus, there is no expectation that the spreads will be comparable to each other.

The range of MACS J0018.5+1626 cluster core initial relative velocity values calculated in this work is $v_i \approx$ 1700–3000 km s^{-1} when the primary and secondary clusters are separated by 3 Mpc. The Li et al. (2020) infall velocities are measured when the subhalo centers are separated by the virial radius of the primary subhalo. We, therefore, calculate for each sampled v_i the corresponding velocity when the clusters are separated by the virial radius of the primary cluster ($v_{r_{200,p}}$ where $r_{200,p} \simeq 1.1$ Mpc). After applying this correction, we find that the analogous range of MACS J0018.5+1626 cluster infall velocity values is $v_{r_{200,p}} \approx$ 3100–4000 km s^{-1}. While this range is, on average, higher than the 2σ range of Li et al. (2020), there is a nonzero overlap between the two distributions. Since our galaxy cluster sample was constructed to maximize the number of high-mass, actively merging systems, we would expect more extreme initial relative velocities on average than in Li et al. (2020). Furthermore, we emphasize that the MACS J0018.5 +1626 cluster core initial relative velocity values are not expected to be exactly equivalent to a rigorously determined posterior probability distribution, and likely yield an underestimation of the true uncertainties since we have not marginalized over all correlations between merger parameters in this analysis due to computational limitations. This comparison indicates that MACS J0018.5+1626 is a reasonably exceptional object relative to those studied by Li et al. (2020), which is in agreement with our selection.

Early hydrodynamical simulation studies designed to reproduce the merger geometry of the Bullet Cluster (e.g., Milosavljević et al. 2007; Springel & Farrar 2007; Mastropietro & Burkert 2008) constrained initial merger parameters by qualitatively matching a handful of characteristic morphological features in mock XSB and total mass distributions to observational data sets. However, none of these works attempted to place uncertainty estimates on the inferred merger parameters. Several works have since improved upon these methods (e.g., Molnar et al. 2012; Lage & Farrar 2014; Chadayammuri et al. 2022). For example, Lage & Farrar (2014) made more quantitative estimates of the Bullet Cluster merger parameters by performing a χ^2 fit between mock and observed data sets. Based on their optimization, Lage & Farrar (2014) characterize an initial relative cluster velocity of the Bullet Cluster in terms of a percent increment relative to the velocity acquired by the clusters while falling in from infinity, with moderate precision ($-10.9\% \pm 15\%$).

Table 6
MACS J0018.5+1626 Merger Parameters Constrained in This Analysis

Parameter	Value(s)
Merger epoch	$0 \lesssim t - t_{\rm peri} \lesssim 60$ Myr
Mass ratio	$R \approx 1.5$–3.0
Impact parameter	$b \lesssim 250$ kpc
Initial[a] relative velocity	$v_i \approx 1700$–3000 km s^{-1}
Viewing angle	$0.77 \lesssim \lvert \boldsymbol{L} \cdot \hat{x} \rvert \lesssim 0.89$[b]
Initial[a] cluster gas profiles	Int+NCC[c]

Notes.
[a] When the cluster components are separated by 3 Mpc.
[b] Inclined ≈27°–40° from the merger axis.
[c] Moderately + strongly disturbed.

In this work, we have systematically compared mock observables from a suite of hydrodynamical simulations to the MACS J0018.5+1626 system with a set of quantitative matching criteria. As a result, we have presented distributions of merger parameters that are consistent with the observed data. In the case of the initial relative velocity, we report this distribution in terms of a physical velocity when the MACS J0018.5+1626 cluster components are separated by 3 Mpc to be ≈1700–3000 km s^{-1} (i.e., corresponding to an approximate fractional uncertainty of 30%). We do not expect these distributions to be exactly equivalent to rigorously determined posterior probability distributions, but we provide these empirically calibrated distributions of likely merger parameters for the first time in such a merger analysis. A summary of all constrained merger parameters for MACS J0018.5+1626 is shown in Table 6.

6. Gas-DM Velocity Decoupling

MACS J0018.5+1626 exhibits a decoupling in projection between the ICM $v_{\rm pec}$ and the $v_{\rm gal}$ maps, which trace the LOS gas and DM velocity structure, respectively. This decoupling manifests as a rotational offset in the POS between the two velocity dipoles of $\Delta\theta_{v,\rm obs} \approx 135$ deg. As described in Section 4.5, we applied a matching criterion enforcing that the mock observables exhibit a similar degree of rotational decoupling in order to determine the MACS J0018.5+1626 merger geometry. In this section, we present a more detailed exploration of this velocity decoupling behavior in the simulations and highlight its dependencies on the merger epoch, viewing angle, and impact parameter.

6.1. Epoch and Viewing Angle

In Figure 11, we provide a simple qualitative 2D schematic of a galaxy cluster merger evolving around the pericenter passage. Since the ICM is affected by collisional processes as the merger progresses, the ICM distribution will begin to lag the DM distribution spatially. When the merger is observed along the merger axis, the ICM and DM velocity dipoles will appear to be well aligned, i.e., $\Delta\theta_{v,\rm obs} \approx 0°$. However, when the

Silich et al.

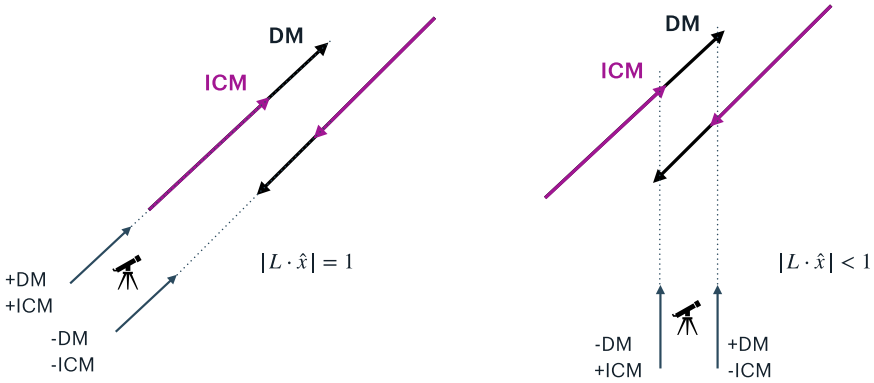

Figure 11. Simple 2D illustration of an induced rotational offset between the DM and ICM velocity dipoles in projection when observed along the merger axis (left) and offset from the merger axis in the plane of the merger (right). In this simple schematic, which assumes only that the ICM distribution lags the DM distribution as the merger evolves near the pericenter passage, the DM/ICM dipole alignment flips from 0° to 180°.

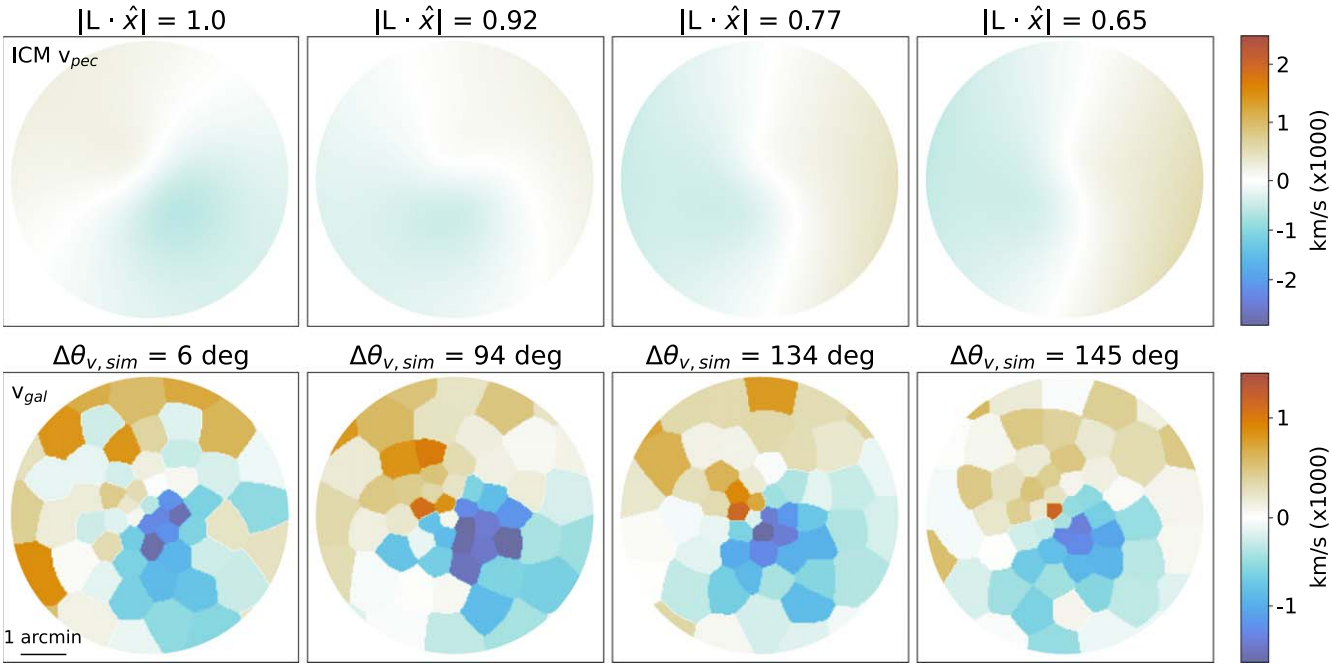

Figure 12. Demonstration of the ICM/DM velocity dipole rotational offset as a function of $|\boldsymbol{L} \cdot \hat{x}|$ for a simulation with $R = 1.5$, $b = 250$ kpc, $v_i = 3000$ km s^{-1}, gas profile: Int+NCC at $t - t_{\rm peri} = 0.02$ Gyr (after pericenter passage). The dipoles are roughly aligned when the viewing angle is aligned with the merger axis, and the magnitude of the rotational offset increases as the viewing angle moves farther from the merger axis.

viewing angle of the system is offset from the merger axis in the plane of the merger, the dipoles become misaligned ($\Delta\theta_{v,\rm obs} \approx 180°$). As the viewing angle moves out of the 2D plane of the merger, we would expect to observe velocity dipole rotational offsets at intermediate angles between 0° and 180°, which we characterize below.

Figure 12 illustrates the dependence of the rotational offset between the ICM and DM LOS velocity dipoles as a function of viewing angle at a fixed epoch for a given set of initial merger parameters. In the full simulation analysis, the components of $\boldsymbol{L}$ are evenly sampled in $\hat{x}$ and randomly sampled in $(\hat{y}, \hat{z})$. To more clearly depict the rotational offset dependence on the viewing angle and minimize effects from merger asymmetries when randomly sampled in $(\hat{y}, \hat{z})$, the viewing angle vector $\boldsymbol{L}$ in this progression is defined to have equal component magnitudes in $(\hat{y}, \hat{z})$ as the component along $\hat{x}$ is varied. At $|\boldsymbol{L} \cdot \hat{x}| = 1$, the velocity dipoles are aligned, and $\Delta\theta_{v,\rm sim}$ increases for viewing angles farther from the merger axis (until the boundary of the sampled parameter space, $|\boldsymbol{L} \cdot \hat{x}| = 0.65$).

The observed rotational offset between the ICM and DM LOS velocity dipoles is further dependent on the merger epoch. In Figure 13, we plot tracks of $\Delta\theta_{v,\rm sim}$ as a function of $|\boldsymbol{L} \cdot \hat{x}|$ at three epochs for the same simulation initialized above. We here identify three tracks in $(\hat{y}, \hat{z})$: where $\boldsymbol{L} \cdot \hat{y} = 0$, $\boldsymbol{L} \cdot \hat{z} = 0$, and where $\boldsymbol{L} \cdot \hat{y} = \boldsymbol{L} \cdot \hat{z}$. This removes any fluctuations between sets of mock observables that could be attributed to a random sampling of merger asymmetries in $(\hat{y}, \hat{z})$. These three tracks indicate that prior to pericenter passage ($t - t_{\rm peri} = -0.2$ Gyr), the DM and ICM LOS velocity dipoles are aligned for all

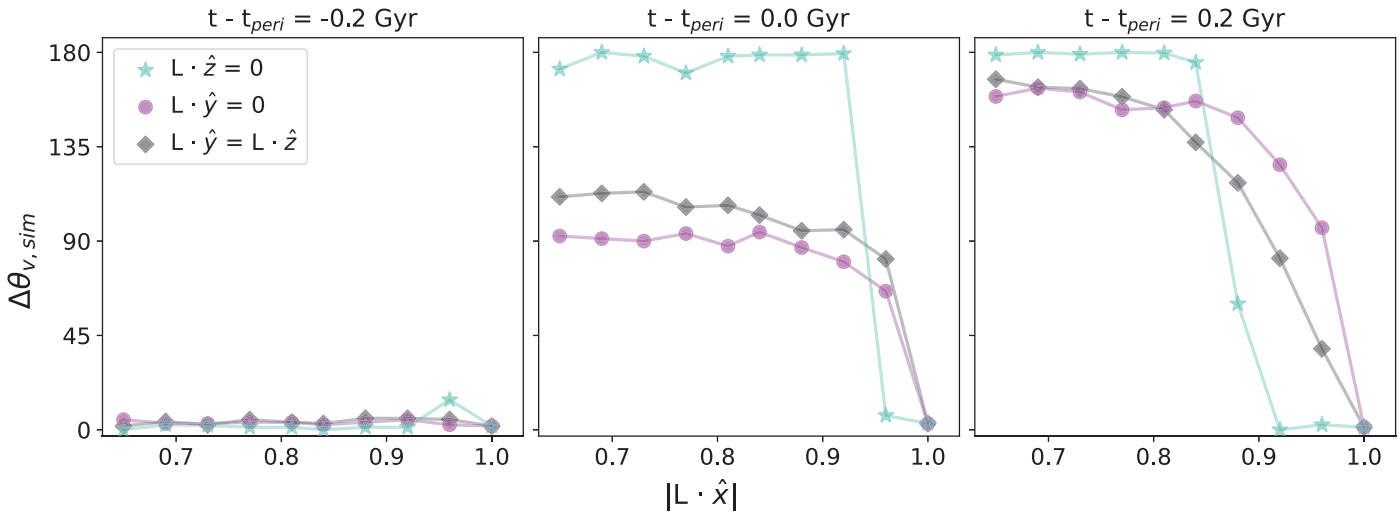

Figure 13. $\Delta\theta_{v,\mathrm{sim}}$ values for simulation snapshots at $t - t_{\mathrm{peri}} = -0.2$ Gyr (left), pericenter passage (center), and $t - t_{\mathrm{peri}} = 0.2$ Gyr (right) as a function of $|L \cdot \hat{x}|$. The simulation was initialized with $R = 1.5$, $b = 250$ kpc, $v_i = 3000$ km s^{-1}, gas profile: Int+NCC. Here, $\Delta\theta_{v,\mathrm{sim}}$ is plotted as an absolute-valued angle from 0° to 180°. Prior to pericenter passage, the DM and ICM LOS velocity dipoles are aligned for all viewing angles. At the pericenter passage epoch, there is an induced rotation of the velocity dipoles and $\Delta\theta_{v,\mathrm{sim}}$ moves from 0° for all $|\boldsymbol{L} \cdot \hat{x}|$, except where $|\boldsymbol{L} \cdot \hat{x}| = 1$. After pericenter passage, the DM and ICM LOS velocity dipoles approach anti-alignment for viewing angles moving farther from the merger axis, while $\Delta\theta_{v,\mathrm{sim}}$ remains ≈0 for $|\boldsymbol{L} \cdot \hat{x}| = 1$. Simulations viewed with larger components of $\boldsymbol{L}$ in $\hat{y}$ exhibit higher degrees of rotation, particularly near pericenter passage.

viewing angles. At the pericenter passage epoch, there is an induced rotation of the velocity dipoles, and $\Delta\theta_{v,\mathrm{sim}}$ moves from 0° for all values of $|\boldsymbol{L} \cdot \hat{x}|$ excepting where $|\boldsymbol{L} \cdot \hat{x}| = 1$ (i.e., looking down the merger axis). There is a further dependence on the specific $(\hat{y}, \hat{z})$ track being followed near the pericenter passage, where simulations viewed with larger components of $\boldsymbol{L}$ in $\hat{y}$ exhibit higher degrees of rotation. After the pericenter passage ($t - t_{\mathrm{peri}} = 0.2$ Gyr), there is a trend toward anti-alignment of the DM and ICM LOS velocity dipoles for viewing angles moving farther from the merger axis (decreasing $|\boldsymbol{L} \cdot \hat{x}|$), while $\Delta\theta_{v,\mathrm{sim}}$ remains ≈0 for $|\boldsymbol{L} \cdot \hat{x}| = 1$.

6.2. Epoch and Impact Parameter

The impact parameter further influences the degree of rotational offset between the ICM and DM LOS velocity dipoles. In Figure 14, we plot distributions of the angular value of the velocity dipole rotational offset as a function of the viewing angle component along the merger axis ($|\boldsymbol{L} \cdot \hat{x}|$) for simulations initialized with each of the sampled impact parameters (with a set of initial conditions reasonably favored by the matching criteria: $R = 1.5$, $v_i = 3000$ km s^{-1}, and gas profile: Int+NCC) at a short range of epochs prior to and post-pericenter passage ($|t - t_{\mathrm{peri}}| \leqslant 100$ Myr). There is rarely any case for which $\Delta\theta_{v,\mathrm{sim}} \neq 0$ for simulations initialized with $b = 250$ kpc and viewed at $|\boldsymbol{L} \cdot \hat{x}| = 1$, in agreement with Figures 12 and 13.

Prior to the epoch of pericenter passage ($-100 \leqslant t - t_{\mathrm{peri}} \leqslant 0$ Myr), simulations initialized with low impact parameters ($b \lesssim 100$ kpc) show a large degree of spatial correlation between the ICM and DM velocity dipoles, i.e., $\Delta\theta_{v,\mathrm{sim}} \approx 0$. The rotational offset is more continuously initialized as the merger approaches pericenter passage for simulations initialized with larger impact parameters. The distributions of $\Delta\theta_{v,\mathrm{sim}}$ for larger sampled impact parameters ($250 \lesssim b \lesssim 500$ kpc) exhibit a broader spread of $\Delta\theta_{v,\mathrm{sim}}$ values in the same short range of epochs prior to pericenter passage ($-100 \leqslant t - t_{\mathrm{peri}} \leqslant 0$ Myr).

In the same range of epochs post-pericenter passage, the transition of the ICM and DM velocity dipoles from well-aligned to anti-aligned happens rapidly (i.e., almost entirely within 100 Myr of the pericenter passage) for low-impact parameter simulations ($b \lesssim 100$ kpc). For simulations initialized with larger impact parameters, ($250 \lesssim b \lesssim 500$ kpc), this transition spreads over intermediate values of $\Delta\theta_{v,\mathrm{sim}}$ much more prominently, and a simple 2D schematic is no longer a good approximation. In Figure 15, we illustrate the evolution of the ICM/DM velocity dipole decoupling as a function of epoch for simulations initialized with impact parameters of $b = 250$ and 500 kpc (with $R = 1.5$, $v_i = 3000$ km s^{-1}, and gas profile: Int+NCC). Here, we utilize the idealized mock observables before any processing in order to highlight the decoupling at the full simulation resolution. Each snapshot is projected along a viewing angle of $|\boldsymbol{L} \cdot \hat{x}| = 0.88$, which is favored by the matching criteria.

For the $b = 250$ kpc simulation, the gas and DM LOS velocity dipoles are aligned at epochs well prior to the pericenter passage (e.g., at $t - t_{\mathrm{peri}} \approx -0.40$ Gyr), with $\Delta\theta_{v,\mathrm{sim}} \approx 0$ (measured as described in Section 4.5). As the $b = 250$ system approaches and undergoes pericenter passage, the DM velocity dipole rapidly rotates, since the DM is governed exclusively by gravitational interactions. The gas dipole rotates more slowly at small radii as the gas undergoes strong collisional interactions, while it remains largely unchanged at large radii. This induces a global DM/ICM velocity dipole offset that reaches ≈145° at $t - t_{\mathrm{peri}} \approx 0.20$ Gyr. As the DM dipole approaches anti-alignment with the original orientation of the dipole, the gas in the inner cluster cores takes several 0.1 Gyr to "catch up" to the DM rotationally, and several additional 0.1 Gyr are required for the rotational motion to propagate outward to large radii, so that the global gas velocity dipole again becomes roughly aligned with the DM velocity dipole by $t - t_{\mathrm{peri}} \approx 0.80$ Gyr.

This general phenomenon is illustrated more dramatically in the $b = 500$ kpc simulation. In this case, the gas and DM velocity dipoles similarly begin aligned ($\Delta\theta_{v,\mathrm{sim}} \approx 0$) at epochs

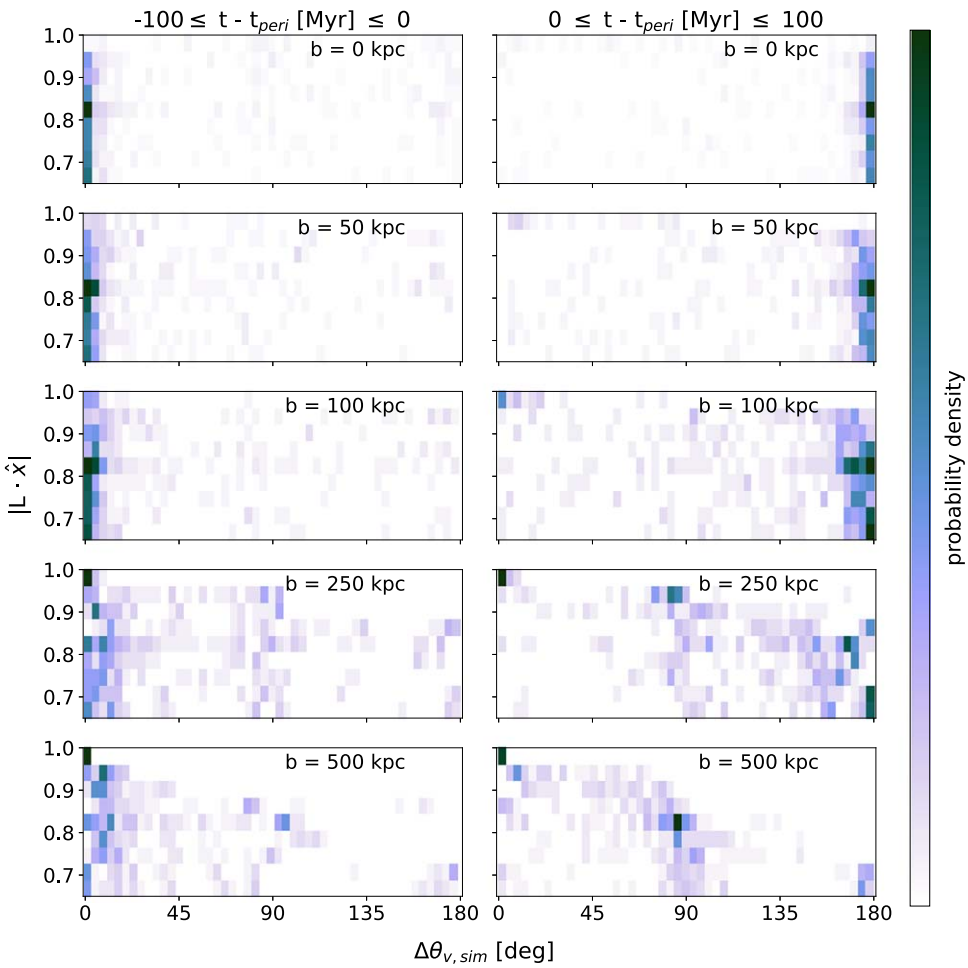

Figure 14. Distributions of $\Delta\theta_{v,\mathrm{sim}}$ as a function of $|\boldsymbol{L}\cdot\hat{x}|$ for simulations initialized with each of the sampled impact parameters ($b = 0$, 50, 100, 250, and 500 kpc) with a set of initial conditions reasonably favored by the matching criteria ($R = 1.5$, $v_i = 3000\,\mathrm{km\,s^{-1}}$, and gas profile: Int+NCC) for epochs prior to and post-pericenter passage ($|t - t_{\mathrm{peri}}| \leqslant 100$ Myr). Simulations initialized with small impact parameters undergo a rapid transition from ICM/DM LOS velocity dipole alignment to anti-alignment with few intermediate rotational offset values. Larger impact parameters exhibit more continuous distributions of $\Delta\theta_{v,\mathrm{sim}}$ from alignment to anti-alignment, and can additionally remain at semi-stable intermediate $\Delta\theta_{v,\mathrm{sim}}$ values that are dependent on the merger viewing angle and impact parameter (e.g., at $\Delta\theta_{v,\mathrm{sim}} \sim 90°$ for $|\boldsymbol{L}\cdot\hat{x}| = 0.84$ and $b = 500$ kpc).

well prior to the pericenter passage. As the $b = 500$ kpc system approaches and undergoes pericenter passage, the DM velocity dipole rapidly rotates toward 180° out of phase with the initial dipole orientation. The gas again rotates more slowly than the DM at the center due to collisional interactions, and it roughly retains its original dipole orientation on large scales. For several 0.1 Gyr post-pericenter passage, the DM velocity dipole approaches and retains an anti-aligned orientation relative to the original DM velocity dipole, and the global gas dipole slowly progresses toward alignment with the DM velocity dipole, with the motion of the outer gas again being driven from the central inner gas outward. As a result, there is a semi-stable rotational offset at $\Delta\theta_{v,\mathrm{sim}} \approx 90°$ for simulations initialized with $b = 500$ kpc and viewed at $|\boldsymbol{L}\cdot\hat{x}| = 0.88$. This is emphasized in Figure 14, where there are pileups of rotational offsets as a function of $|\boldsymbol{L}\cdot\hat{x}|$, particularly for large impact parameters.

These trends persist regardless of the sign of $|\boldsymbol{L}\cdot\hat{x}|$ and for simulations that are projected along viewing angles sampled an order of magnitude more finely in $|\boldsymbol{L}\cdot\hat{x}|$. Movies sampled more finely in epoch space illustrating this velocity decoupling, in addition to the evolution of the gas temperature and the gas/DM densities, are shown for the above cases in Figures B1 and B2.

7. Conclusions

In this work, we have demonstrated the constraining power of the ICM-SHOX pipeline to jointly infer multiple galaxy cluster merger parameters quantitatively via comparison of a novel combination of multi-probe observables to mock observables generated from idealized hydrodynamical simulations tailored to the MACS J0018.5+1626 merger. We constrain the MACS J0018.5+1626 cluster component masses and gas profiles, as well as global system properties: viewing angle, epoch, initial impact parameter, and initial relative velocity. The epoch is likely in the range of 0–60 Myr after the pericenter passage, and the viewing angle is likely inclined ≈27°–40° from the merger axis along which the relative velocity between the cluster components is initialized when the clusters are separated by 3 Mpc at the initial infall. The most likely MACS J0018.5+1626 impact parameter is $b \lesssim 250$ kpc, the mass ratio is $R \approx 1.5$–3.0, the initial relative velocity is $v_i \approx 1700$–$3000\,\mathrm{km\,s^{-1}}$, and the primary and secondary cluster

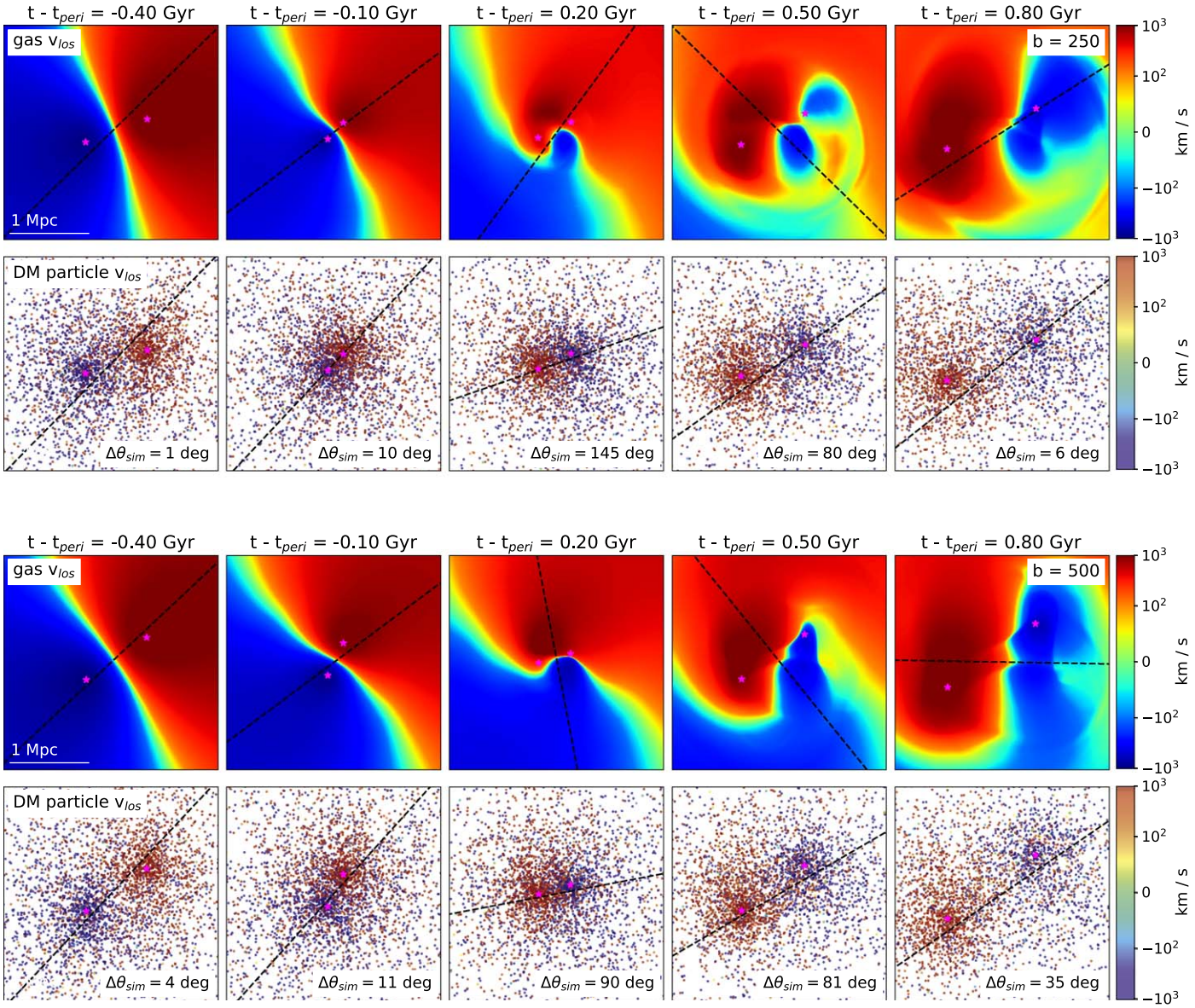

Figure 15. Evolution of the ICM/DM LOS velocity dipole decoupling (measured as $\Delta\theta_{v,\mathrm{sim}}$) as a function of epoch for simulations initialized with impact parameters of $b = 250$ (top) and 500 kpc (bottom), with $R = 1.5$, $v_i = 3000$ km s^{-1}, and gas profile: Int+NCC for each simulation. Mock velocity maps are shown at the full simulation resolution with black dashed lines indicating the calculated rotational orientation of each velocity dipole. Prior to the pericenter passage, the velocity dipoles are well aligned. As the merger progresses, the DM velocity dipole rotates more quickly than the ICM velocity dipole, which lags the DM velocity dipole in the inner regions before catching up and then propagating outward over several 0.1 Gyr post-pericenter passage, when the large-scale dipoles again approach alignment. This leads to a continuous sampling of intermediate rotational offset values, including angles that are semi-stable for some geometries (e.g., values near $\sim 90°$ in the bottom example for $b = 500$ kpc).

components initially have gas distributions that are moderately and strongly disturbed, respectively.

Our application of the ICM-SHOX pipeline to MACS J0018.5+1626 has revealed a most curious observable: a misalignment of the velocity maps of the gas and the stellar components of the merging system. This misalignment is manifested by a separation in phase space between DM and ICM LOS velocity maps generated with cluster-member z_{spec} and kSZ, respectively, which our simulations indicate is entirely dependent on the different collisional properties of the gas, DM, and stars. The decoupling is initiated as the clusters approach the pericenter passage when the ICM begins to be affected by merger-driven hydrodynamical processes, while the DM does not. Systematically, the behavior of the velocity space decoupling is, therefore, highly sensitive to the merger epoch, system geometry, and the orientation of the merger relative to our LOS. Such a discovery would not be possible without our multi-probe approach, especially incorporating the kSZ measurements, and its interpretation would be difficult without careful comparison to simulations.

In this demonstration of the ICM-SHOX multi-probe data and pipeline, we identified a set of matching criteria that were manually calibrated on each MACS J0018.5+1626 cluster observable (e.g., distance between GL mass peaks). However, due to the low S/N of the ICM v_{pec} map, identifying a categorical matching criterion was not feasible, and we thus developed a more formal statistical comparison for the ICM v_{pec} map. In future studies, we plan to apply this methodology to the full set of multi-probe data by empirically calibrating a simulated χ^2 distribution for each mock observable. By

utilizing these distributions, we can more objectively determine the matching thresholds without relying on the human eye to identify patterns in the observables. After implementing these improvements, we plan to apply this framework to the full ICM-SHOX sample.

Acknowledgments

Some of the data presented herein were obtained at the W. M. Keck Observatory, which is operated as a scientific partnership among the California Institute of Technology (Caltech), the University of California, and the National Aeronautics and Space Administration (NASA). The Observatory was made possible by the generous financial support of the W. M. Keck Foundation. The authors wish to recognize and acknowledge the very significant cultural role and reverence that the summit of Maunakea has always had within the indigenous Hawaiian community. We are most fortunate to have the opportunity to conduct observations from this mountain.

The X-ray observations in this analysis were obtained from the Chandra Data Archive. The hydrodynamical simulations were run on the Pleiades supercomputer at NASA/Ames Research Center. The simulation post-processing computations were conducted in the Resnick High Performance Computing Center, a facility supported by the Resnick Sustainability Institute at Caltech.

E.M.S. acknowledges support from a National Science Foundation Graduate Research Fellowship (NSF GRFP) under grant No. DGE-1745301, the Wallace L. W. Sargent Graduate Fellowship at Caltech, and NSF/AST-2206082. J.S. acknowledges support from NSF/AST-2206082. J.A.Z. and U.C. are funded by the Chandra X-ray Center, which is operated by the Smithsonian Astrophysical Observatory for and on behalf of NASA under contract NAS8-03060. E.B. acknowledges support from NSF/AST-2206083. A.Z. acknowledges support by grant No. 2020750 from the United States-Israel Binational Science Foundation (BSF) and grant No. 2109066 from the United States NSF, and by the Ministry of Science & Technology, Israel. T.M. acknowledges support from the AtLAST project, which has received funding from the European Union's Horizon 2020 research and innovation program under grant agreement No 951815. A.M. thanks support from Consejo Nacional de Humanidades Ciencias y Technologías (CONAHCYT) project A1-S-45680. We thank the anonymous reviewer for the detailed comments, which helped improve this manuscript.

Facilities: Keck/DEIMOS, CXO, CSO, ASTE (installed on the 10 m Atacama Submillimeter Telescope Experiment), Planck, HST.

Software: `GAMER-2` (Schive et al. 2018), `Xspec` 12.12.0 (Arnaud 1996), `yt` (Turk et al. 2011), `pyXSIM` (ZuHone & Hallman 2016), SOXS (ZuHone et al. 2023), `mpi4py` (Dalcin & Fang 2021), `CIAO` (Fruscione et al. 2006), `PypeIt` (Prochaska et al. 2020), `spec2d` (Cooper et al. 2012; Newman et al. 2013), `SpecPro` (Masters & Capak 2011), `Pumpkin` (Rhea et al. 2020), Astropy (Astropy Collaboration et al. 2013, 2018), `NumPy` (van der Walt et al. 2011; Harris et al. 2020), Matplotlib (Hunter 2007), `lmfit` (Newville et al. 2014), `Colossus` (Diemer 2018), `contbin` (Sanders 2006), `scikit-image`; (van der Walt et al. 2014).

Appendix A
Merger Progression Movie

Figure A1 shows an example evolution of mock galaxy cluster merger observables as a function of epoch.

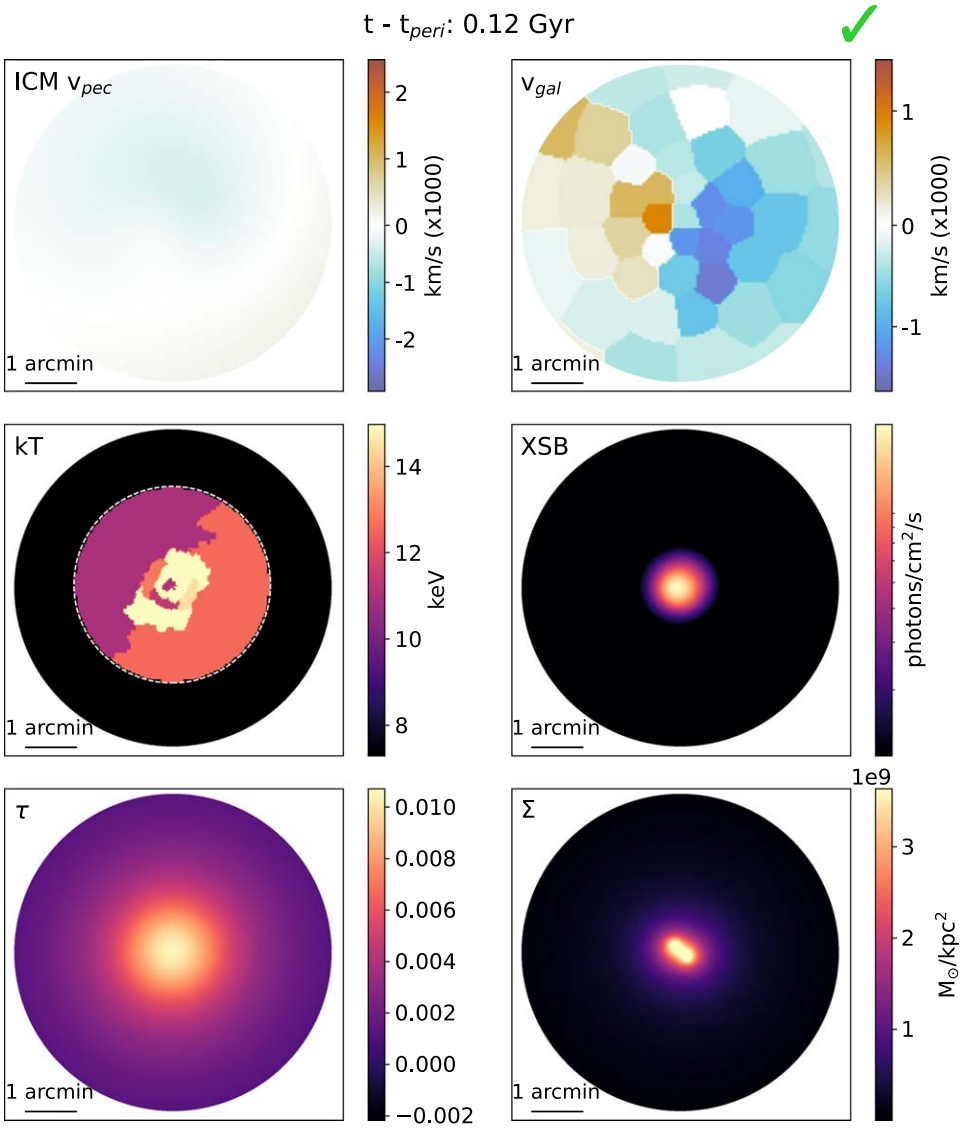

Figure A1. Simulated cluster merger progression as a function of epoch for a simulation initialized with $R = 1.5$, $b = 250$ kpc, $v_i = 1700$ km s^{-1}, gas profile: Int +NCC, and $|\boldsymbol{L} \cdot \hat{x}| = 0.92$. The red "X" or green check mark in the top right corner indicates whether or not a given snapshot passes the matching criteria. Those that pass the matching criteria correspond to epochs near the pericenter passage, when the mock observables best resemble the MACS J0018.5+1626 observational data. (An animation of this figure is available.)

Appendix B
Velocity Decoupling Movies

Figures B1 and B2 show example simulated evolutions of the ICM/DM velocity dipole decoupling.

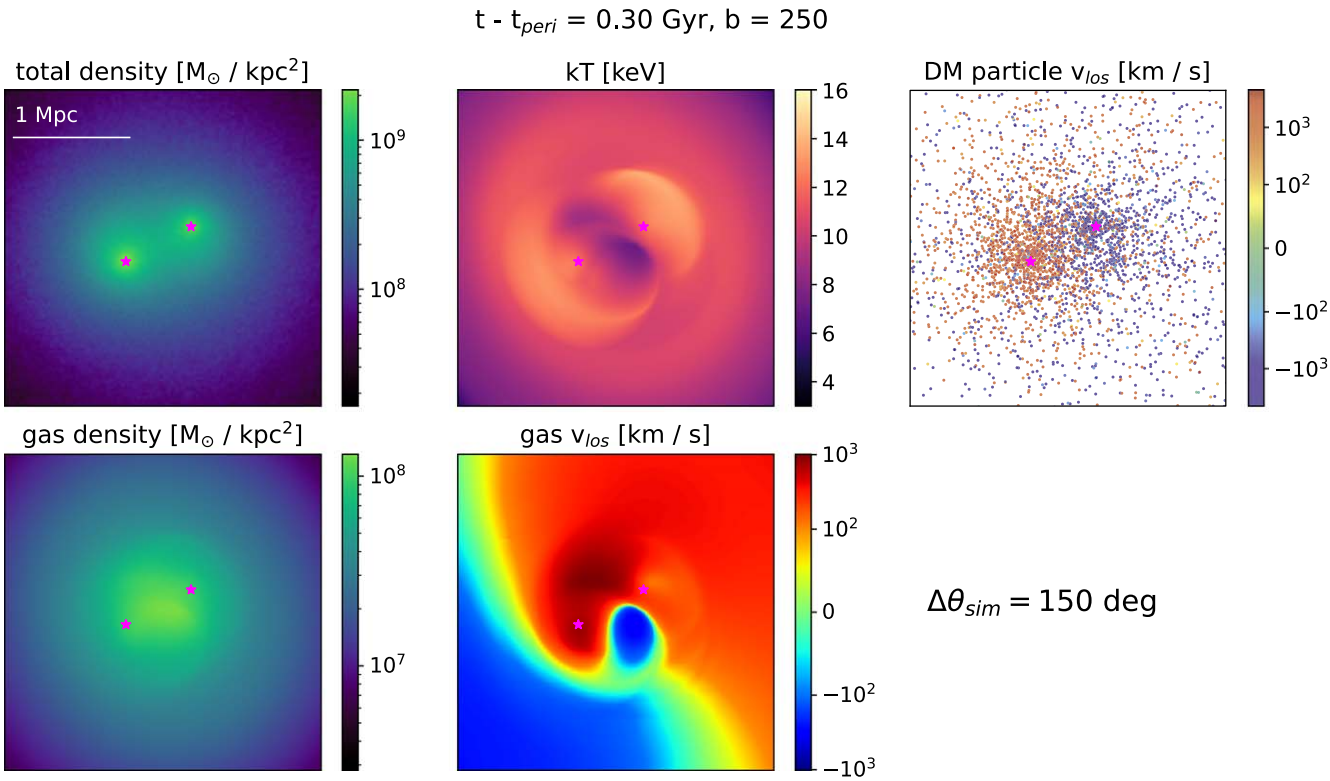

Figure B1. Simulated evolution of the ICM/DM velocity dipole decoupling, as well as the total/gas densities and gas temperature, as a function of epoch for simulations initialized with $b = 250$, $R = 1.5$, $v_i = 3000$ km s^{-1}, and gas profile: Int+NCC viewed at $|\boldsymbol{L} \cdot \hat{x}| = 0.88$. Each mock map is shown at the full simulation resolution for clarity. Prior to the pericenter passage, the velocity dipoles are aligned ($\Delta\theta_{v,\mathrm{sim}} \approx 0$). As the merger progresses, the DM velocity dipole in the inner regions rotates more quickly than the ICM velocity dipole, which lags the DM velocity dipole. The gas velocity dipole catches up to the DM velocity dipole within several 0.1 Gyr post-pericenter passage, and several additional 0.1 Gyr are required for the rotational gas motion to propagate outward to large radii, so that the global gas velocity dipole again becomes roughly aligned with the DM velocity dipole by $t - t_{\mathrm{peri}} \approx 0.80$ Gyr.

(An animation of this figure is available.)

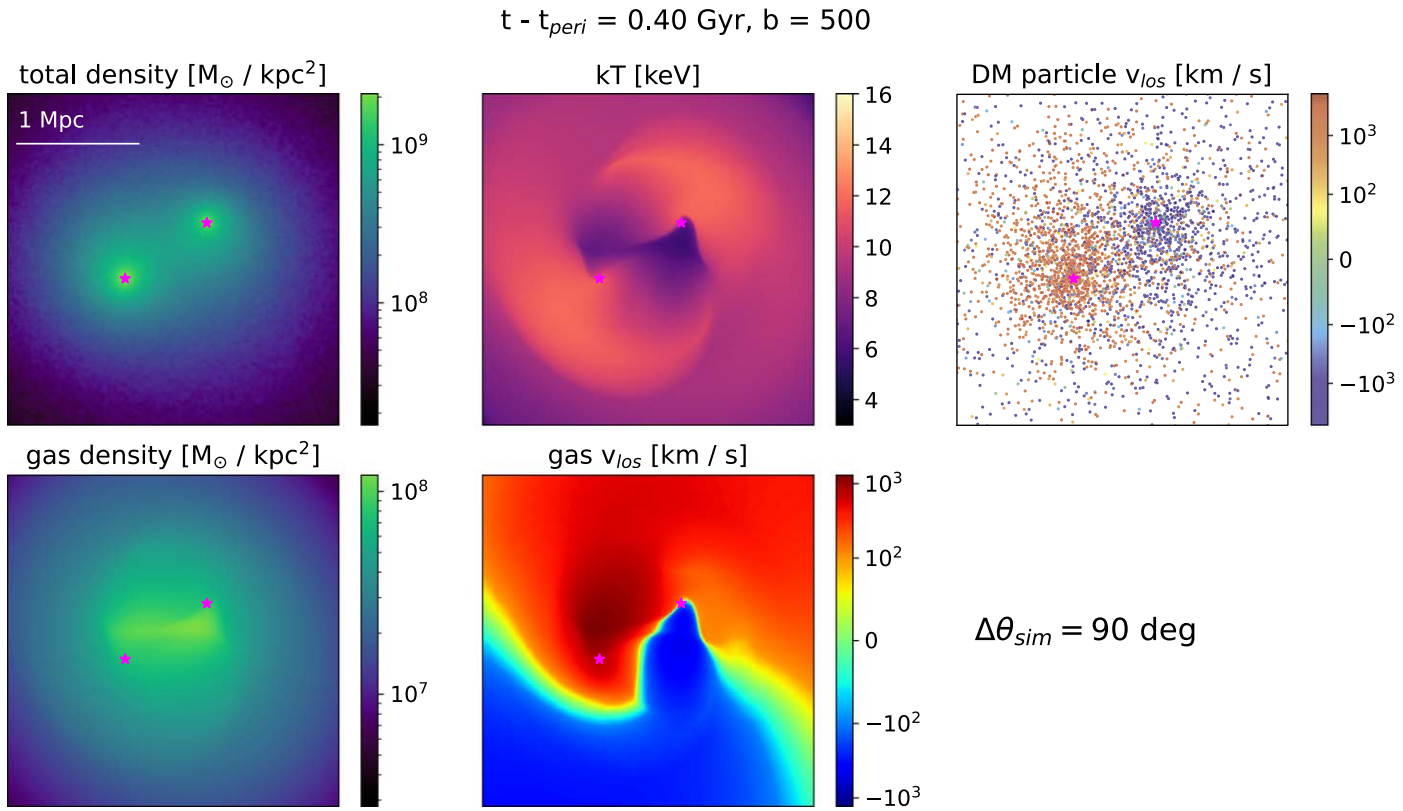

Figure B2. Simulated evolution of the ICM/DM velocity dipole decoupling, as well as the total/gas densities and gas temperature, as a function of epoch for simulations initialized with $b = 500$, $R = 1.5$, $v_i = 3000$ km s^{-1}, and gas profile: Int+NCC viewed at $|\boldsymbol{L} \cdot \hat{x}| = 0.88$. Each mock map is shown at the full simulation resolution for clarity. Prior to the pericenter passage, the velocity dipoles are aligned ($\Delta\theta_{v,\mathrm{sim}} \approx 0$). As the merger progresses, the DM velocity dipole in the inner regions rotates more quickly than the ICM velocity dipole, which lags the DM velocity dipole. The gas velocity dipole catches up to the DM velocity dipole within several 0.1 Gyr post-pericenter passage, and as the rotational gas motions propagate outward to large radii, there is a semi-stable rotational offset at $\Delta\theta_{v,\mathrm{sim}} \approx 90°$ for several 0.1 Gyr post-pericenter passage before reaching an offset of $\approx 20°$ by $t - t_{\mathrm{peri}} \approx 0.80$ Gyr.

(An animation of this figure is available.)

Appendix C
Spectroscopic Redshifts

Tables C1–C3 contain the relevant literature cluster-member redshifts, as well as (non-) cluster-member redshifts that were observed in our Keck program for MACS J0018.5+1626.

Table C1
Literature Cluster-member Spectroscopic Redshifts for MACS J0018.5+1626.

R.A.	Decl.	z	Reference	Duplicate
$00^h18^m01.^s63$	$+16°27'01.''02$	0.5515	Crawford et al. (2011)	⋯
$00^h18^m03.^s83$	$+16°24'16.''13$	0.5410	Crawford et al. (2011)	⋯
$00^h18^m05.^s98$	$+16°27'26.''28$	0.5536	Crawford et al. (2011)	⋯
$00^h18^m06.^s66$	$+16°26'56.''73$	0.5658	Crawford et al. (2011)	⋯
$00^h18^m06.^s84$	$+16°24'27.''81$	0.5500	Crawford et al. (2011)	⋯

Note. Objects that are observed as duplicates, and therefore excluded from our analysis, are indicated. Only objects within a $6.'7 \times 6.'7$ region centered on the cluster center are used in the v_{gal} map generation.
References. Crawford et al. (2011), Dressler & Gunn (1992), Ellingson et al. (1998).

(This table is available in its entirety in machine-readable form.)

Table C2
Cluster-member Spectroscopic Redshifts for MACS J0018.5+1626 Observed with DEIMOS in Our Keck Program

R.A.	Decl.	z	Observation Date	Duplicate
$00^h17^m59.^s90$	$+16°33'06.''00$	0.5645	2021 Aug 16	⋯
$00^h18^m02.^s56$	$+16°17'34.''60$	0.5416	2020 Aug 13	⋯
$00^h18^m02.^s69$	$+16°17'22.''70$	0.5539	2020 Aug 13	⋯
$00^h18^m08.^s32$	$+1°18'05.''30$	0.5507	2020 Aug 13	⋯
$00^h18^m08.^s77$	$+16°30'26.''90$	0.5455	2021 Aug 16	⋯

Note. Objects that are observed as duplicates, and therefore excluded from our analysis, are indicated. Only objects within a $6.'7 \times 6.'7$ region centered on the cluster center are used in the v_{gal} map generation.

(This table is available in its entirety in machine-readable form.)

Table C3
Non-cluster-member Spectroscopic Redshifts Observed with DEIMOS in Our Keck Program

R.A.	Decl.	z	Observation Date
$00^h18^m00.^s17$	$+16°32'50.''60$	0.3295	2021 Aug 16
$00^h18^m01.^s19$	$+16°34'55.''90$	0.4750	2021 Aug 16
$00^h18^m03.^s04$	$+16°30'54.''50$	0.2375	2021 Aug 16
$00^h18^m03.^s37$	$+16°34'11.''30$	0.7404	2021 Aug 16
$00^h18^m03.^s44$	$+16°32'06.''90$	0.4870	2021 Aug 16

Note. These redshifts were not used in the analysis, but we include this table for completeness.

(This table is available in its entirety in machine-readable form.)

ORCID iDs

Emily M. Silich https://orcid.org/0000-0002-1616-5649
Elena Bellomi https://orcid.org/0000-0001-6411-3686
Jack Sayers https://orcid.org/0000-0002-8213-3784
John ZuHone https://orcid.org/0000-0003-3175-2347
Sunil Golwala https://orcid.org/0000-0002-1098-7174
Alfredo Montaña https://orcid.org/0000-0003-4229-381X
Tony Mroczkowski https://orcid.org/0000-0003-3816-5372
Daisuke Nagai https://orcid.org/0000-0002-6766-5942
David Sánchez-Argüelles https://orcid.org/0000-0002-7344-9920
S. A. Stanford https://orcid.org/0000-0003-0122-0841
Grant Wilson https://orcid.org/0000-0003-2705-9152
Michael Zemcov https://orcid.org/0000-0001-8253-1451
Adi Zitrin https://orcid.org/0000-0002-0350-4488

References

Adam, R., Bartalucci, I., Pratt, G. W., et al. 2017, A&A, 598, A115
Anbajagane, D., Aung, H., Evrard, A. E., et al. 2022, MNRAS, 510, 2980
Anders, E., & Grevesse, N. 1989, GeCoA, 53, 197
Araya-Melo, P. A., Reisenegger, A., Meza, A., et al. 2009, MNRAS, 399, 97
Arnaud, K. A. 1996, in ASP Conf. Ser. 101, Astronomical Data Analysis Software and Systems V, ed. G. H. Jacoby & J. Barnes (San Francisco, CA: ASP), 17
Astropy Collaboration, Price-Whelan, A. M., Sipőcz, B. M., et al. 2018, AJ, 156, 123
Astropy Collaboration, Robitaille, T. P., Tollerud, E. J., et al. 2013, A&A, 558, A33
Baltz, E. A., Marshall, P., & Oguri, M. 2009, JCAP, 2009, 015
Barret, D., Decourchelle, A., Fabian, A., et al. 2020, AN, 341, 224
Bartalucci, I., Mazzotta, P., Bourdin, H., & Vikhlinin, A. 2014, A&A, 566, A25
Beers, T. C., Flynn, K., & Gebhardt, K. 1990, AJ, 100, 32
Boschin, W., Girardi, M., & Barrena, R. 2013, MNRAS, 434, 772
Boschin, W., Girardi, M., Spolaor, M., & Barrena, R. 2006, A&A, 449, 461
Breuer, J. P., Werner, N., Mernier, F., et al. 2020, MNRAS, 495, 5014
Cavagnolo, K. W., Donahue, M., Voit, G. M., & Sun, M. 2009, ApJS, 182, 12
Chadayammuri, U., ZuHone, J., Nulsen, P., et al. 2022, MNRAS, 509, 1201
Clowe, D., Bradač, M., Gonzalez, A. H., et al. 2006, ApJL, 648, L109
Coe, D. 2016, Reionization Lensing Cluster Survey ("RELICS"), STScI/MAST, doi:10.17909/T9SP45
Coe, D., Salmon, B., Bradač, M., et al. 2019, ApJ, 884, 85
Cooper, M. C., Newman, J. A., Davis, M., Finkbeiner, D. P., & Gerke, B. F., 2012 spec2d: DEEP2 DEIMOS Spectral Pipeline, Astrophysics Source Code Library, ascl:1203.003
Crawford, S. M., Wirth, G. D., Bershady, M. A., & Hon, K. 2011, ApJ, 741, 98
Dalcin, L., & Fang, Y.-L. L. 2021, CSE, 23, 47
Dehghan, S., Johnston-Hollitt, M., Colless, M., & Miller, R. 2017, MNRAS, 468, 2645
Di Mascolo, L., Mroczkowski, T., Perrott, Y., et al. 2021, A&A, 650, A153
Diehl, S., & Statler, T. S. 2006, MNRAS, 368, 497
Diemer, B. 2018, ApJS, 239, 35
Diemer, B., & Joyce, M. 2019, ApJ, 871, 168
Dressler, A., & Gunn, J. E. 1992, ApJS, 78, 1
Ebeling, H., Barrett, E., Donovan, D., et al. 2007, ApJL, 661, L33
Eddington, A. S. 1916, MNRAS, 76, 572
Ellingson, E., Yee, H. K. C., Abraham, R. G., Morris, S. L., & Carlberg, R. G. 1998, ApJS, 116, 247
Faber, S. M., Phillips, A. C., Kibrick, R. I., et al. 2003, Proc. SPIE, 4841, 1657
Fakhouri, O., Ma, C.-P., & Boylan-Kolchin, M. 2010, MNRAS, 406, 2267
Freeman, P. E., Kashyap, V., Rosner, R., & Lamb, D. Q. 2002, ApJS, 138, 185
Fruscione, A., McDowell, J. C., Allen, G. E., et al. 2006, Proc. SPIE, 6270, 62701V
Furtak, L. J., Plat, A., Zitrin, A., et al. 2022, MNRAS, 516, 1373
Harris, C. R., Millman, K. J., van der Walt, S. J., et al. 2020, Natur, 585, 357
HI4PI Collaboration, Ben Bekhti, N., Flöer, L., et al. 2016, A&A, 594, A116
Hitomi Collaboration, Aharonian, F., Akamatsu, H., et al. 2016, Natur, 535, 117
Hitomi Collaboration, Aharonian, F., Akamatsu, H., et al. 2018, PASJ, 70, 9
Hunter, J. D. 2007, CSE, 9, 90
Kaiser, N. 1986, MNRAS, 222, 323
Kazantzidis, S., Magorrian, J., & Moore, B. 2004, ApJ, 601, 37
Kraft, R., Markevitch, M., Kilbourne, C., et al. 2022, arXiv:2211.09827
Kravtsov, A. V., & Borgani, S. 2012, ARA&A, 50, 353
Lacey, C., & Cole, S. 1993, MNRAS, 262, 627
Lage, C., & Farrar, G. 2014, ApJ, 787, 144
Landau, L. D., & Lifshitz, E. M. 1959, Fluid Mechanics (Oxford: Pergamon Press)
Li, Z.-Z., Zhao, D.-H., Jing, Y. P., Han, J., & Dong, F.-Y. 2020, ApJ, 905, 177
Ma, C.-J., Ebeling, H., & Barrett, E. 2009, ApJL, 693, L56
Mantz, A., Allen, S. W., Ebeling, H., Rapetti, D., & Drlica-Wagner, A. 2010, MNRAS, 406, 1773
Markevitch, M., Gonzalez, A. H., David, L., et al. 2002, ApJL, 567, L27
Markevitch, M., & Vikhlinin, A. 2007, PhR, 443, 1
Masters, D., & Capak, P. 2011, PASP, 123, 638
Mastropietro, C., & Burkert, A. 2008, MNRAS, 389, 967
Merten, J., Coe, D., Dupke, R., et al. 2011, MNRAS, 417, 333
Milosavljević, M., Koda, J., Nagai, D., Nakar, E., & Shapiro, P. R. 2007, ApJL, 661, L131
Molnar, S. 2016, FrASS, 2, 7
Molnar, S. M., Hearn, N. C., & Stadel, J. G. 2012, ApJ, 748, 45
Mroczkowski, T., Nagai, D., Basu, K., et al. 2019, SSRv, 215, 17
Muldrew, S. I., Hatch, N. A., & Cooke, E. A. 2015, MNRAS, 452, 2528
Nagai, D., Kravtsov, A. V., & Vikhlinin, A. 2007, ApJ, 668, 1
Newman, J. A., Cooper, M. C., Davis, M., et al. 2013, ApJS, 208, 5
Newville, M., Stensitzki, T., Allen, D. B., & Ingargiola, A. 2014, LMFIT: Non-Linear Least-Square Minimization and Curve-Fitting for Python, v0.8.0, Zenodo, doi:10.5281/zenodo.11813
Owers, M. S., Randall, S. W., Nulsen, P. E. J., et al. 2011, ApJ, 728, 27
Piffaretti, R., Jetzer, P., & Schindler, S. 2003, A&A, 398, 41
Planck Collaboration, Aghanim, N., Akrami, Y., et al. 2020, A&A, 641, A6
Poole, G. B., Fardal, M. A., Babul, A., et al. 2006, MNRAS, 373, 881
Prochaska, J., Hennawi, J., Westfall, K., et al. 2020, JOSS, 5, 2308
Rhea, C., Hlavacek-Larrondo, J., Perreault-Levasseur, L., Gendron-Marsolais, M.-L., & Kraft, R. 2020, AJ, 160, 202
Ricker, P. M., & Sarazin, C. L. 2001, ApJ, 561, 621
Russell, H. R., McNamara, B. R., Sanders, J. S., et al. 2012, MNRAS, 423, 236
Russell, H. R., Nulsen, P. E. J., Caprioli, D., et al. 2022, MNRAS, 514, 1477
Sanders, J. S. 2006, MNRAS, 371, 829
Sanders, J. S., Fabian, A. C., Russell, H. R., Walker, S. A., & Blundell, K. M. 2016a, MNRAS, 460, 1898
Sanders, J. S., Fabian, A. C., Taylor, G. B., et al. 2016b, MNRAS, 457, 82
Sayers, J., Montaña, A., Mroczkowski, T., et al. 2019, ApJ, 880, 45
Sayers, J., Mroczkowski, T., Zemcov, M., et al. 2013, ApJ, 778, 52
Schive, H.-Y., ZuHone, J. A., Goldbaum, N. J., et al. 2018, MNRAS, 481, 4815
Smith, R. K., Brickhouse, N. S., Liedahl, D. A., & Raymond, J. C. 2001, ApJL, 556, L91
Solovyeva, L., Anokhin, S., Sauvageot, J. L., Teyssier, R., & Neumann, D. 2007, A&A, 476, 63
Springel, V., & Farrar, G. R. 2007, MNRAS, 380, 911
Springel, V., White, S. D. M., Jenkins, A., et al. 2005, Natur, 435, 629
Sunyaev, R. A., & Zeldovich, I. B. 1980, MNRAS, 190, 413
Thompson, R., Davé, R., & Nagamine, K. 2015, MNRAS, 452, 3030
Thompson, R., & Nagamine, K. 2012, MNRAS, 419, 3560
Turk, M. J., Smith, B. D., Oishi, J. S., et al. 2011, ApJS, 192, 9
van der Walt, S., Colbert, S. C., & Varoquaux, G. 2011, CSE, 13, 22
van der Walt, S., Schönberger, J. L., Nunez-Iglesias, J., et al. 2014, PeerJ, 2, e453
van Weeren, R. J., Röttgering, H. J. A., Brüggen, M., & Hoeft, M. 2010, Sci, 330, 347
Vikhlinin, A., Kravtsov, A., Forman, W., et al. 2006, ApJ, 640, 691
Voit, G. M. 2005, RvMP, 77, 207
Wilms, J., Allen, A., & McCray, R. 2000, ApJ, 542, 914
XRISM Science Team 2020, arXiv:2003.04962
Zitrin, A., Broadhurst, T., Barkana, R., Rephaeli, Y., & Benítez, N. 2011, MNRAS, 410, 1939
Zitrin, A., Fabris, A., Merten, J., et al. 2015, ApJ, 801, 44
ZuHone, J. A. 2011, ApJ, 728, 54
ZuHone, J. A., & Hallman, E. J., 2016 pyXSIM: Synthetic X-ray Observations Generator, Astrophysics Source Code Library, ascl:1608.002
ZuHone, J. A., Kowalik, K., Öhman, E., Lau, E., & Nagai, D. 2018, ApJS, 234, 4
ZuHone, J. A., Vikhlinin, A., Tremblay, G. R., et al., 2023 SOXS: Simulated Observations of X-ray Sources, Astrophysics Source Code Library, ascl:2301.024